

1 **Intraseasonal modulation of Sea Surface Temperatures in the** 2 **Tropical North Atlantic by African Easterly Waves**

3 Marc K. Mendy ^{1,2}, Florent Gasparin ², Manon Gévaudan ³, Moussa Diakhaté ², Issa Sakho ²,
4 Julien Jouanno ¹

5 ¹ Université de Toulouse, LEGOS (IRD/UT3/CNES/CNRS), Toulouse, France,

6 ² Université Amadou Mahtar Mbow, Diarniadio, Sénégal,

7 ³ Centre National de Recherches Météorologiques, CNRM-CNRS, Météo-France, Toulouse, France

8 *Correspondence to:* Marc K. Mendy (marckakantemendy@gmail.com)

9 **Abstract.** The sea surface temperature (SST) variability in the Tropical North Atlantic (TNA) plays a
10 crucial role in the regional climate by modulating the Intertropical Convergence Zone (ITCZ) and
11 influencing precipitation, convective systems, and tropical cyclones. While atmospheric synoptic-scale
12 intraseasonal variability in this region is dominated by African Easterly Waves (AEWs), their impact
13 on SST remains poorly understood. This study investigates the modulation of SST by AEWs using a
14 regional configuration of a coupled ocean-atmosphere model and moored surface buoy air-sea
15 observations. The results reveal a significant AEWs signature in SST anomalies, with typical
16 temperature fluctuations of approximately ± 0.3 °C (reaching up to ± 0.5 °C for the strongest events). A
17 heat budget analysis shows that AEWs mainly influence SST through modulation of the latent heat flux,
18 shortwave radiation, and vertical mixing. The contribution of the ocean mixing and that of the air-sea
19 fluxes appear of similar order. The dominant 3–5-day AEWs exhibit a stronger impact than their 6–9-
20 day counterparts. These findings highlight the role of AEWs in driving SST variability and mixed-layer
21 dynamics, underscore the importance of accurately representing them in coupled climate models, and
22 call for further investigation into their influence on the mean and seasonal upper-ocean state.

23 1 Introduction

24 The variability of the sea surface temperature (SST) in the Tropical North Atlantic (TNA) is a key factor
25 in determining the regional climate and affects surrounding countries. It plays a critical role in
26 modulating the position of the Intertropical Convergence Zone (ITCZ) (Wane et al., 2021), as shown by
27 the strong correlation between the ITCZ and the regions of highest SST (zonal band of $SST \geq 27^\circ\text{C}$)
28 (Graham and Barnett, 1987; Waliser and Graham, 1993; Opoku-Ankomah and Cordery, 1994). This
29 variability plays a key role in establishing and maintaining convective systems and precipitation in the
30 tropical Atlantic, West Africa, and northeastern South America (Moura and Shukla, 1981; Hastenrath
31 and Greischar, 1993; Nobre and Shukla, 1996; Sultan and Janicot, 2000; Nicholson, 2009; Tomaziello
32 et al., 2016). Furthermore, the frequency and intensity of tropical cyclones, which draw their energy
33 from the warm waters of the Tropical Atlantic, are influenced by these SST anomalies (Emanuel, 2005;
34 Webster et al., 2005). Therefore, a better understanding of the mechanisms involved in SST variability
35 is essential not only to enhance our comprehension of climate processes, but also to reduce SST biases
36 in coupled models and refine climate forecasts.

37 At the synoptic scale, atmospheric variability in this region is predominantly governed by African
38 Easterly Waves (AEWs) (Thompson et al., 1979; Diedhiou et al., 2001). These are westward-
39 propagating atmospheric disturbances with periods ranging from 2 to 10 days, which develop during the
40 boreal summer over the tropical region, primarily across West Africa. AEWs generally originate from
41 atmospheric instabilities, particularly barotropic-baroclinic instabilities associated with the African
42 Easterly Jet (Burpee, 1972). They also originate from convection, which not only facilitates their
43 initiation but can also enhance their growth (Berry and Thorncroft, 2005; Mekonnen et al., 2006;
44 Thorncroft et al., 2008; Russell et al., 2020). AEWs are generally classified into two period bands: 3-5
45 days and 6-9 days (Diedhiou et al., 1998a, b, 1999; Felice et al., 1990, 1993; Wu et al., 2013). The 3-5
46 days AEWs propagate preferentially on either side of the African Easterly Jet, before merging over the
47 Atlantic, generally at around 17.5°N . They have average-zonal wavelengths of around 3,000 km and
48 phase speeds of up to 10 m/s (Diedhiou et al., 1998a; Reed et al., 1988; Thorncroft and Hodges, 2001).
49 Those of 6 to 9 days, further north and more intermittent, unfold with an average phase speed of around
50 6 m/s and wavelengths of around 5000 km (Diedhiou et al., 2010; Wu et al., 2013).

51 On their trajectory, AEWs interact closely with deep convection, playing a central role in modulating
52 atmospheric dynamics in West Africa. Several studies have highlighted the influence of AEWs on the
53 organization, intensity and propagation of mesoscale convective systems (Berry and Thorncroft, 2005;
54 Kiladis et al., 2006; Russell et al., 2020). In particular, these interactions are manifested by an
55 amplification of convection in cyclonic convergence zones associated with wave troughs, thus
56 promoting the triggering or intensification of precipitation (Fink and Reiner, 2003; Kiladis et al., 2006).
57 Moreover, under certain favorable conditions, particularly when deep convection persists downstream

58 of the wave, these systems can contribute to the cyclogenesis process in the TNA (Thorncroft and
59 Hodges, 2001; Dunkerton et al., 2009; Russell et al., 2017; Bercos-Hickey and Patricola, 2025).

60 In the Tropical North Pacific, Mickett et al. (2010), using a slab model and comparing surface wind-
61 induced inertial kinetic energy fluxes in the mixed layer, show that these waves (Pacific Easterly Waves,
62 PEWs) resonantly force inertial motions, which influence sea surface temperatures. In their recent work,
63 Hummels et al. (2020) put forward the hypothesis that, in the TNA, AEWs would contribute to cooling
64 the ocean surface, through the associated latent heat fluxes, and the strong vertical mixing at the base of
65 the mixed layer induced by the near-inertial waves they would generate. However, their importance of
66 AEWs in the regional heat balance, and consequently on surface temperature, remains to be clarified.
67 While numerous studies have investigated the characteristics of AEWs and their role in climate
68 modulation, to our knowledge no study has yet examined their impact on ocean surface conditions in
69 the Tropical Atlantic. Using a coupled ocean–atmosphere configuration of the Tropical Atlantic
70 (Gévaudan et al., 2021), the aim of this study is to examine whether AEWs influence SST in this region
71 and investigate the underlying mechanisms.

72 The paper is organized as follows: the Tropical Atlantic coupled model and the validation datasets are
73 presented in Section 2. A comparison of model and observations of SST and winds associated with
74 AEWs is provided in Section 3. Section 4 examines the ocean surface response to AEWs by projecting
75 a representative AEWs index, derived from near-surface winds, onto SST. Section 5 investigates the
76 underlying mechanisms based on the analysis of the ocean heat balance in the surface layer. Finally, the
77 conclusion and perspectives are provided in Section 6.

78 **2 Data and methodological approach**

79 **2.1 Regional coupled model**

80 This study is based on a regional configuration of the coupled NEMO-WRF model sharing the same
81 horizontal grid at a resolution of $\frac{1}{4}^\circ$ (Δx and $\Delta y \sim 27$ km) for the tropical Atlantic (99°W - 20°E , 15°S -
82 35°N) (Gévaudan et al., 2021, 2022). These two models interact on an hourly basis, exchanging SST,
83 surface currents, surface stress, air-sea surface fluxes, and freshwater fluxes via the OASIS coupler. The
84 parameterization follows that of Gévaudan et al. (2021), with updates to align it with more recent
85 versions of the various codes: NEMO-v4.2.1 (Madec et al., 2023) and WRF-v4.2.1 (Skamarock et al.,
86 2019). The models are coupled using OASIS3-MCT V4.0 (Valcke and Redler, 2012; Craig et al., 2017).

87 The ocean model solves the three-dimensional primitive equations, has 75 fixed vertical levels (z
88 coordinates), with 12 levels in the upper 20 m and 24 levels in the upper 100 m. Lateral open boundaries
89 of the model are prescribed using an interannual hindcast of temperature, salinity, sea level and
90 horizontal velocities from the MERCATOR global daily reanalysis GLORYS2V4 (Ferry et al., 2012).
91 To include ocean color in the solar radiation penetration scheme, the model is driven by daily

92 chlorophyll concentrations from GlobColour 009_082, derived from several satellite products
93 (Maritorena et al., 2010; Garnesson et al., 2019). The atmospheric model WRF solves the compressible,
94 non-hydrostatic Euler equations using the Advanced Research WRF (ARW) dynamical solver. It
95 employs a grid with 40 terrain-following vertical levels (sigma coordinates), with the top of the
96 atmosphere set at 50 hPa. Lateral boundary conditions are given by 3-hourly atmospheric fields from
97 the ERA5 reanalysis from the European Centre for Medium-Range Weather Forecasts (ECMWF)
98 (Hersbach et al., 2020). Vertical mixing in the ocean model is parameterized using the Generic Length
99 scale (GLS) turbulence closure in a k- ϵ configuration (Reffray et al., 2015).

100 The ocean model was initialized on January 1, 2000, based on a forced NEMO simulation of 20 years
101 (1980-1999). The atmospheric model was initialized from ERA5 reanalysis on January 1, 2000. The
102 coupled model is spun up for one year (2000), then run over a 21-year period (2001–2021), producing
103 daily outputs of oceanic and atmospheric fields. To investigate the processes that drive the SST
104 variations associated with AEWs, the different contributions to the 3D temperature balance are
105 computed online at each grid point and saved daily (details are given in Section 5).

106 **2.2 Validation datasets**

107 To validate the simulations, a variety of datasets covering the period from 2001 to 2021 were used.
108 These include the ERA5 reanalysis, which uses advanced modelling and data assimilation systems to
109 combine vast amounts of historical observations with global estimates (Hersbach et al., 2020). For this
110 study, the 10-m surface winds (u_{10} and v_{10}), the winds along the atmospheric column (u and v) and the
111 daily available SST at $1/4^\circ$ were used to validate the performance of our model in reproducing the
112 dynamics and thermodynamics in our study area. In addition, winds measured by the Advanced
113 SCATterometer (ASCAT), which is on board the operational meteorological satellite MetOp, are used.
114 These data are available on a $1/4^\circ$ horizontal grid with a daily time step since 2007 (J. Figa-Saldaña and
115 Stoffelen, 2002).

116 The model's SST is also compared to NOAA's Optimum Interpolation Sea Surface Temperature
117 (OISST) version 2.0, which is a combination of satellite observations (AVHRR), in-situ measurements
118 from ships and buoys (including PIRATA), adjusted to fill gaps by optimal interpolation (Reynolds et
119 al., 2007; Banzon et al., 2016). These data are available at $1/4^\circ$ resolution and daily frequency from late
120 1981 to the present, and represent a blended bulk SST product. Finally, daily wind at 4 m and surface
121 temperature measured at 1 m depth derived from the entire PIRATA mooring array (Bourlès et al., 2019)
122 in the TNA were also used to validate the model. Wind measurements from PIRATA buoy are reported
123 at an anemometer height of 4 m ($Wind_{4m}$) and are scaled to 10-m wind speed ($Wind_{10m}$) to ensure
124 consistency with ERA5, ASCAT, and the model diagnostics. The conversion is performed using a
125 neutral logarithmic wind profile:

126

$$\text{Wind}_z = \frac{u_*}{\kappa} \ln\left(\frac{z}{z_0}\right),$$

127

128

129

130

131

132

133

134

135

136

Where u_* is the friction velocity, κ is the von Kármán constant, z is the height above the surface, and z_0 is the aerodynamic roughness length. A representative open-ocean roughness length of $z_0 = 2 \times 10^{-4}$ m is assumed. This value of surface roughness length (z_0) is consistent with commonly reported values under moderate wind conditions ([Charnock, 1955](#); [Dutton, 1986](#); [Fairall et al., 2003](#); [Fleagle and Businger, 1981](#); [Large and Pond, 1981](#)) Sensitivity tests show that using plausible open-ocean values of z_0 (order $10^{-4} - 10^{-3}$) changes the 4-10 m wind conversion factor by only ~ 1 -2% relative to our reference value, corresponding typically ~ 0.05 - 0.15 $\text{m}\cdot\text{s}^{-1}$ for wind speeds of 5 - 10 $\text{m}\cdot\text{s}^{-1}$. In addition, a small uncertainty in the reported anemometer height would produce a similarly modest effect on the conversion factor. These uncertainties remain small compared to the synoptic wind variability considered in this study.

137

2.3 Identification of AEWs

138

139

140

141

142

143

144

To identify AEWs, we apply a 4th-order zero-phase Butterworth band-pass filter to the time series, retaining variability in the 2–10-day period. The filter is applied using a forward–backward procedure, which removes phase distortion while preserving the amplitude of the signal. This range is widely used in the literature as it encompasses the typical synoptic variability associated with AEWs ([Russell et al., 2017](#); [Danso et al., 2022](#); [Jonville et al., 2025](#)). Although we use the “2–10-day” denomination, the upper cutoff frequency of the filter is set slightly below the Nyquist frequency ($0.99 \times \text{Nyquist}$) to account for the daily sampling.

145

146

147

148

149

150

151

152

153

154

155

This method to detect AEWs involves applying temporal filtering techniques (here Butterworth filter) to the target variables to isolate the part associated with AEWs. Other approaches, such as spectral analysis ([Wheeler and Kiladis, 1999](#); [Fink and Reiner, 2003](#); [Jiang et al., 2023](#)) and Lagrangian tracking methods ([Carlson, 1969](#); [Thorncroft and Hodges, 2001](#)) are also used to detect AEWs. These techniques make it possible to track the spatio-temporal evolution of AEWs troughs and identify their implications in modulating local climate. However, in the output fields of mesh models or reanalysis, temporal filtering remains a robust method for isolating AEWs signals over large domains ([Skinner and Diffenbaugh, 2013](#); [Jonville et al., 2024](#)). We focus on the July–August–September (JAS) period, which is widely used in the literature to study AEWs ([Janiga and Thorncroft, 2013](#); [Bercos-Hickey et al., 2017](#); [Semunegus et al., 2017](#); [Raj et al., 2023](#)), as it corresponds to the peak season of AEWs activity over West Africa and the tropical Atlantic ([Grist, 2002](#)).

156

157

158

To quantify the impact of AEWs on atmospheric and oceanic variables, we employ a linear regression framework to band-pass filtered anomaly time series. An AEW index is defined from the filtered 10m meridional wind over a reference region characterized by strong synoptic variability.

159

160

The AEW index is not normalized prior to regression, so that the regression coefficients retain their physical units and can be directly interpreted as the response per m/s of 10-m meridional wind anomaly.

161 Regressions are performed independently at each grid point using ordinary least squares. For a given
162 variable $y(t)$, the regression against the AEW index $x(t)$ is expressed as:

$$163 \quad y(t + \Delta t) = a \cdot x(t) + b + \epsilon(t)$$

164 where a is the regression slope, b is the intercept, ϵ the residual, and Δt a prescribed time lag. Lagged
165 regressions are implemented by shifting the dependent variable in time relative to the AEW index,
166 allowing the temporal evolution of the atmospheric and oceanic response throughout the AEW life cycle
167 to be examined.

168 To facilitate the interpretation of the regression results, the regression coefficients are evaluated for a
169 representative AEW amplitude derived directly from the AEW index (i.e., meridional wind). The local
170 extremes of the filtered index are identified, and only peaks exceeding one standard deviation in absolute
171 value ($|x| > 1\sigma$) are retained, thus isolating robust and well-developed AEW events while excluding
172 weak fluctuations. The representative AEW amplitude is defined as the average magnitude of these
173 peaks.

174 This threshold corresponds to synoptic-scale meridional wind anomalies with typical amplitudes of 4.45
175 m/s. More restrictive thresholds were also tested (e.g., $|x| > 2\sigma$), which isolate only the most intense
176 AEW events and are associated with larger wind anomalies (averaging around 6.5 m/s). These sensitivity
177 tests amplify the signal but do not modify the spatial structure of the regression patterns and are therefore
178 not discussed further. Statistical significance is assessed independently at each grid point using the
179 student's t-test for the regression slope, with p-values obtained directly from the regression analysis.
180 Only regression coefficients that are significant at the 95% confidence level ($p < 0.05$) are retained and
181 displayed in the figures. Given that temporal filtering introduces autocorrelation and reduces the
182 effective number of degrees of freedom, this significance threshold should be considered conservative.
183 The robustness of the results is therefore mainly assessed through the spatial consistency of the
184 regression models and their consistency between variables and time lags, in line with current practice in
185 studies on synoptic-scale variability (Russell et al., 2017; Skinner and Diffenbaugh, 2013).

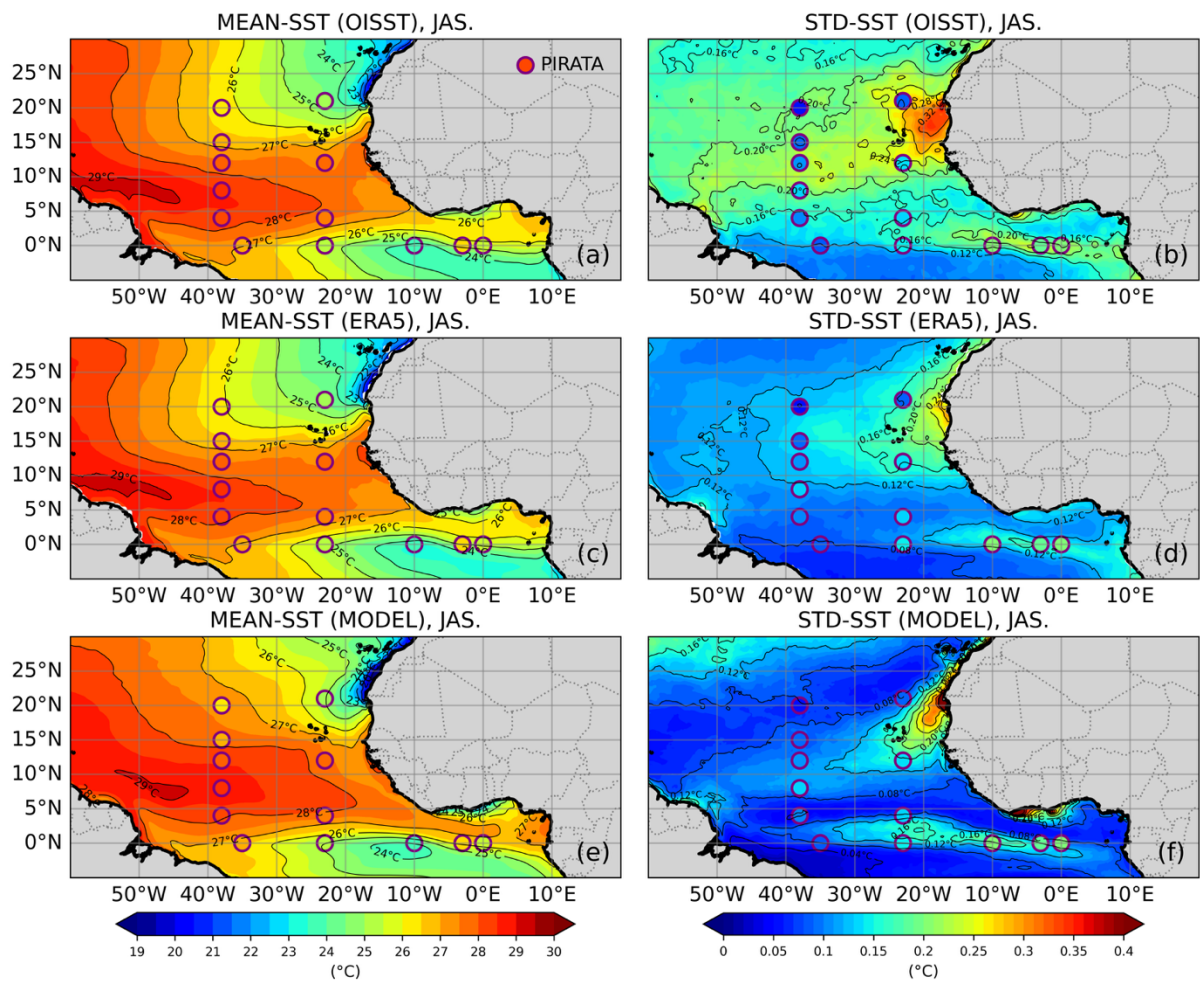
186 **3 Evaluation of the coupled model**

187 First, we assess the model's ability to reproduce AEWs and surface ocean conditions. To this end, we
188 focus on both the mean state and the high-frequency variability of key variables: SST, surface wind at
189 10 m, and the vertical wind structure along 20°W.

190 **3.1 Sea surface temperature**

191 The mean SST and the standard deviation of SST anomalies filtered between 2 and 10 days are shown
192 in Figure 1 for OISST, ERA5, PIRATA, and the coupled model. Overall, the coupled model realistically
193 reproduces the large-scale spatial distribution of mean SST over the tropical Atlantic. In the western
194 part of the basin, the Atlantic Warm Pool, which is defined as the area where SSTs exceed 28°C during

195 boreal summer (Enfield and Lee, 2005; Wang et al., 2006, 2008), extends slightly further east in the
 196 model than in ERA5, OISST or PIRATA moorings. Along the African coast, between 21°N and 25°N,
 197 the model represents well the cool SSTs associated with the Mauritanian upwelling system. Southeast
 198 of the Equator, the Atlantic cold tongue is clearly identified, with SSTs around 24°C during the boreal
 199 summer. This feature is commonly attributed to Ekman divergence induced by the southeast trade winds
 200 crossing the Equator (Cromwell, 1953; Stommel, 1959), together with enhanced vertical turbulent
 201 mixing in the eastern tropical Atlantic (Jouanno et al., 2011a; Wade et al., 2011). While the overall
 202 structure of the cold tongue is well represented by the coupled model, a modest warm bias persists in
 203 the eastern tropical Atlantic. This is a well-documented characteristic of climate simulations in this
 204 region (Shi et al., 2018; Voldoire et al., 2019; Deppenmeier et al., 2020). Nevertheless, the bias in the
 205 coupled model is weaker than in state-of-the-art models.

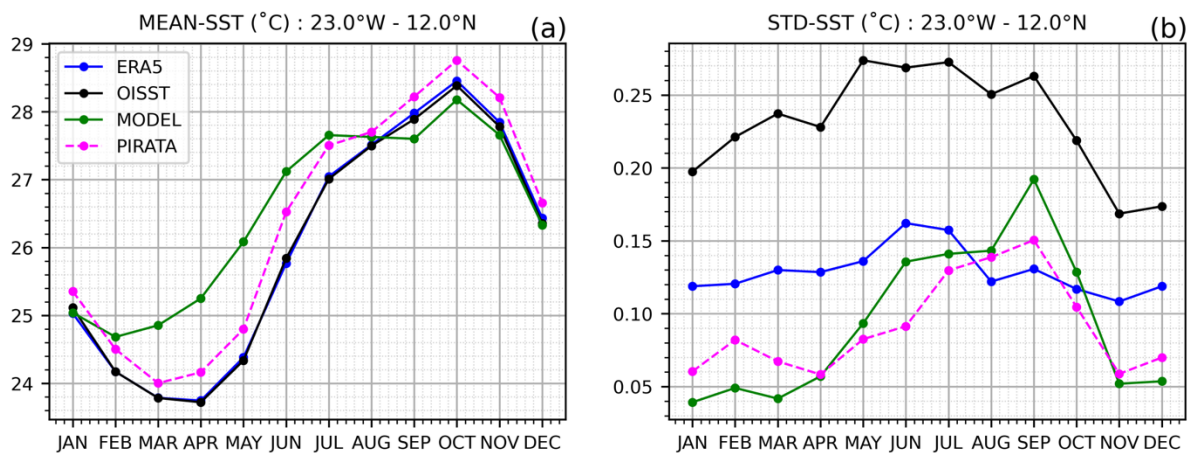


206
 207 **Figure 1: (Left panels) Mean SST, and (right panels) standard deviation of SST anomalies for July–August–**
 208 **September (JAS) over the 2007–2021 period, from (a), (b) OISST, (c), (d) ERA5, and (e), (f) the coupled**
 209 **model. The standard deviation is computed from anomalies band-pass filtered in the 2–10-day range. In**
 210 **each panel, estimates from the PIRATA mooring are indicated by circles.**

211 The standard deviation of SST anomalies filtered in the 2–10-day band reveals substantial amplitude
 212 differences among the various products (Fig. 1b,d,f). OISST exhibits larger synoptic variability than the
 213 other datasets, while ERA5 shows comparatively weaker variability at these time scales. Differences in
 214 synoptic SST variability among OISST, ERA5, and the coupled model likely arise from a combination
 215 of factors, including analysis methodology, spatial smoothing, and effective temporal sampling, as
 216 documented in previous intercomparisons of SST products (e.g., Huang et al., 2021; Reynolds et al.,
 217 2007). Previous studies also have shown that ocean surface temperatures can be particularly sensitive to
 218 high-frequency atmospheric forcings, such as variations in wind speed, cloud cover and radiative fluxes,
 219 particularly at timescales of less than a week (Murray et al., 2000; Donlon et al., 2002)

220 To assess the realism of synoptic SST variability, we place particular emphasis on comparisons with in
 221 situ observations from PIRATA moorings, which provide SST measurements at a depth of
 222 approximately 1 m and are consistent with the vertical resolution and daily averaging of the coupled
 223 model. This comparison indicates that the coupled model reproduces the amplitude and spatial
 224 distribution of SST variability over the 2-to-10-day band better than ERA5 (Fig. 1d, f).

225 In particular, the coupled model accurately reproduces two regions of high synoptic variability in SST
 226 observed by PIRATA: a zonal band along the northern front of the Atlantic cold tongue, between 0°N
 227 and 5°N, and a south-westerly band further north, between 10° and 20°N. These structures are also
 228 present in the other datasets, although their amplitude varies. The coupled model's ability to reproduce
 229 these observed configurations confirms its relevance for studying the response of the ocean surface to
 230 synoptic atmospheric variability, particularly AEWs, in the tropical Atlantic.

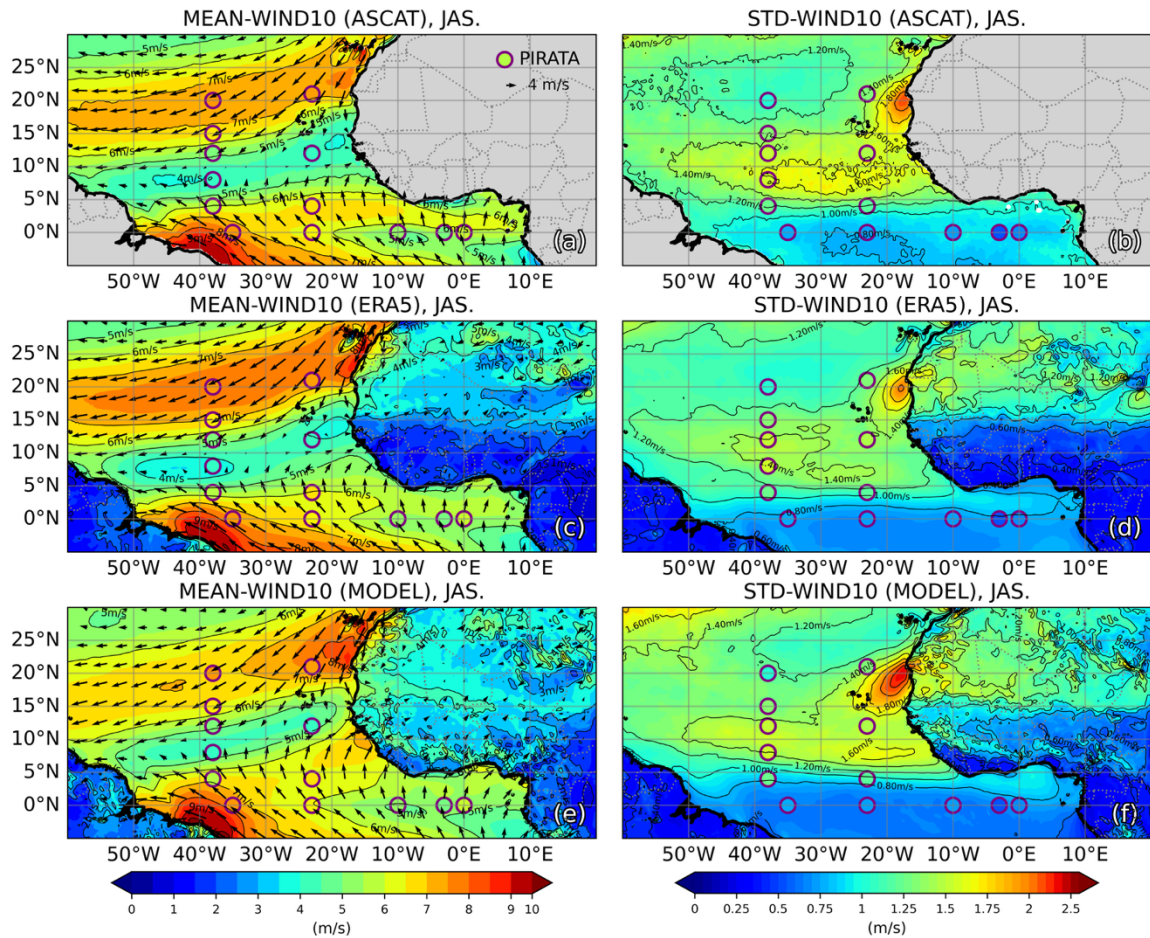


231
 232 **Figure 2: (a) Monthly climatology of SST, and (b) standard deviation of SST anomalies at 23°W–12°N over**
 233 **the 2007–2021 period of OISST (black), ERA5 (blue), the coupled model (green), and the 23°W–12°N**
 234 **PIRATA mooring (pink). Anomalies are band-pass filtered in the 2–10-day range prior to computing the**
 235 **standard deviation.**

236 Figure 2 presents the SST climatology (from 2007 to 2021) and the standard deviation of SST anomalies
237 filtered in the 2–10-day band for different datasets at 23°W-12°N, corresponding to the location of a
238 PIRATA mooring in a region of high variability in SST (Fig. 1f). The seasonal cycle of SST is broadly
239 consistent across the different estimates (Fig. 2a). The model has a warm bias of about 1°C relative to
240 PIRATA from March to May, while biases during the rest of the year remain smaller than 0.5°C.
241 However, larger differences are observed in the amplitude of high-frequency variability in SST (Fig.
242 2b), which is consistent with the spatial patterns identified in Figures 1b, 1d and 1f. OISST exhibits
243 significantly higher variability over a 2- to 10-day period than the other products, while ERA5 displays
244 low variability and weak seasonal modulation. The coupled model, on the other hand, agrees well with
245 PIRATA observations, reproducing both the amplitude and the seasonal cycle of synoptic SST
246 variability, with a marked maximum during the boreal summer (JAS). This specific comparison supports
247 the use of PIRATA observations as the primary reference for assessing high frequency SST variability
248 and confirms the ability of the coupled model to represent this variability in the region.

249 **3.2 10-meter winds**

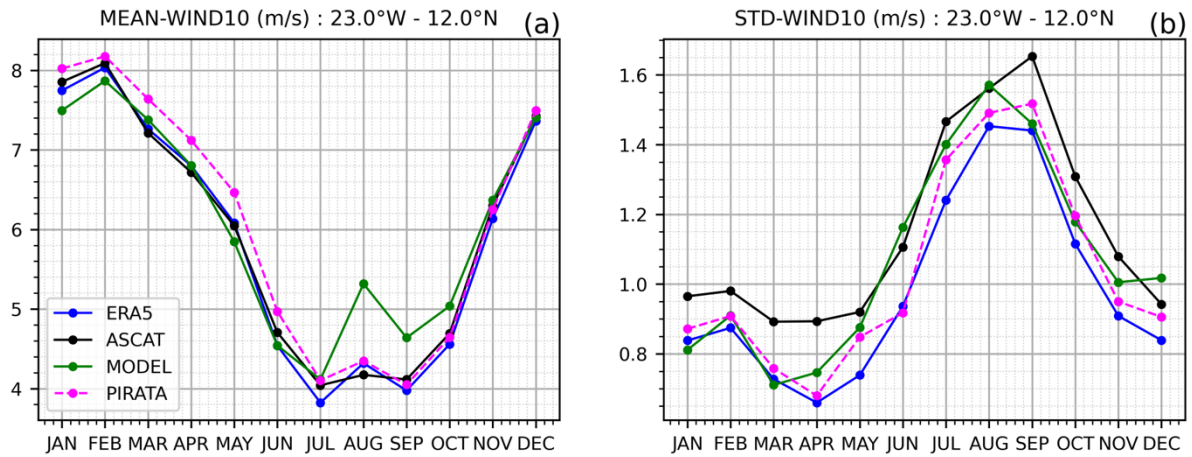
250 We now assess the ability of the model to reproduce surface wind conditions by comparing 10-m winds
251 from the coupled model with those from ERA5, the ASCAT scatterometer, and in-situ PIRATA
252 measurements. Figure 3 presents the mean 10-m wind (speed and direction) and the standard deviation
253 of anomalies band-pass filtered in the 2–10-day range for the JAS period. On average, the different
254 products show the convergence of the trade winds from the North-East and South-East towards the
255 region of maximum SST (here > 27°C, Fig. 1), which appears to be a response of the winds to the SST
256 anomalies (Sweet et al., 1981; Wallace et al., 1989). This pattern defines the ITCZ, located west of
257 30°W and around 8°N at this time of year. The ITCZ then tilts northward (between 10°N and 15°N) in
258 the eastern tropical Atlantic, following the SST maximum (Gill, 1980). South of the equator, the
259 southeasterly trade winds cross the equator and are then deflected to the right by the Coriolis force,
260 giving rise to south-westerly winds north of the equator. Laden with moisture, these winds bring the
261 West African monsoon to the continent during the northern summer. These characteristics are very well
262 reproduced by the coupled model, despite a slight positive bias (< 0.5m/s) compared to ASCAT. ERA5
263 winds are closer to PIRATA and ASCAT in the vicinity of the ITCZ and along the West African coast,
264 while slightly weaker winds are found over other parts of the basin. Exhibiting a pattern similar to the
265 2–10-day SST variability (Fig. 1), the 10-m wind variability is pronounced along the West African coast
266 and extends offshore. The largest amplitudes are found off Senegal and Mauritania, where the standard
267 deviation reaches values of up to about 2m/s, consistent with the strong synoptic modulation of the low-
268 level flow in this region.



269

270 **Figure 3: 10-m wind speed for the months of July-August-September (left panels) and corresponding**
 271 **standard deviation (right panels) over the 2007–2021 period for (a), (b) ASCAT, (c), (d) ERA5 and (e), (f)**
 272 **the coupled model. The standard deviation is computed from anomalies filtered in the 2–10-day band. In**
 273 **each panel, PIRATA mooring values are indicated by circles.**

274 The monthly climatology of the 10-m wind and the corresponding standard deviation of anomalies in
 275 the 2–10-day frequency band are shown in Figure 4 for the model, ERA5, ASCAT and the PIRATA
 276 mooring at 23°W-12°N. A clear seasonal cycle is evident in all datasets, with minimum wind speeds
 277 during boreal summer associated with the passage of the ITCZ, and maximum values in winter. The
 278 different products exhibit similar seasonal fluctuations, with mean wind speed differences generally
 279 smaller than 0.5 m/s. The 2–10-day variability of the wind at 10 m peaks in summer, consistent with
 280 enhanced AEW activity, and shows only minor differences among the datasets, typically below 0.2 m/s.



281

282 **Figure 4: (a) Monthly climatology and (b) monthly standard deviation of the 10-m wind speed at 23°W–**
 283 **12°N over the 2007–2021 period for ASCAT (black), ERA5 (blue), the coupled model (green), and the 23°W–**
 284 **12°N PIRATA mooring. The standard deviation is computed from anomalies filtered in the 2–10-day band.**

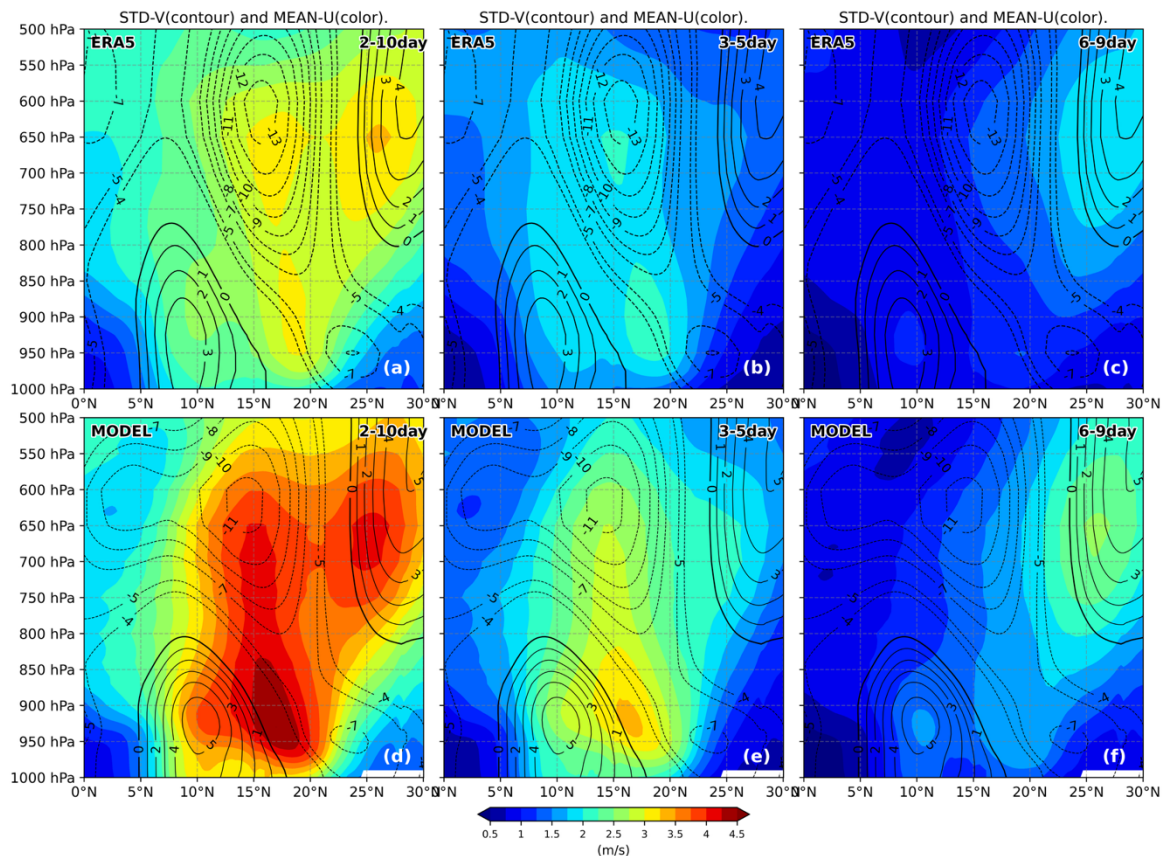
285 3.3 Vertical wind structure

286 In this region, wind variability on timescales of 2 to 10 days is largely driven by AEWs. However, this
 287 range is quite broad, and it is well known that there are actually two distinct regimes, which we will
 288 refer to as southern and northern AEWs, each characterized by different vertical structures, periods, and
 289 horizontal distributions (Diedhiou et al., 1998b, 1999; Felice et al., 1990; Viltard et al., 1997). The
 290 objective here is to assess whether the model can accurately capture both types of AEWs: those with
 291 periods of 3–5 days (hereafter AEW_{S3-5day}) and those with periods of 6–9 days (hereafter AEW_{S6-9day}).

292 Figure 5 presents a meridional section of the mean zonal wind (shown as contours) and the standard
 293 deviation of the meridional wind anomalies (shown as shading) for the ERA5 reanalysis and the coupled
 294 model. Meridional wind anomalies are band-pass filtered in the range of 2–10 day, as well as separately
 295 in the 3–5 day and 6–9 day bands, and the results are zonally averaged between 25°W and 15°W during
 296 JAS period over 2001–2021. Overall, the coupled model reproduces the large-scale vertical structure of
 297 the atmospheric circulation reasonably well, exhibiting spatial patterns similar to those in ERA5 data.
 298 However, the model produces a stronger wind signal than ERA5, with differences around 1 m/s for the
 299 mean zonal wind and about 1.25 m/s for the standard deviation of the meridional wind. The African
 300 Easterly Jet is clearly distinguishable, with its core located near 600 hPa and 15°N, and wind speeds of
 301 13 m/s in ERA5 and 11 m/s in the coupled model. At the level of the African Easterly Jet, two maxima
 302 of meridional wind variability are observed: around 15°N for AEW_{S3-5day} and around 25°N for AEW_{S6-9day}.
 303 A maximum of meridional wind variability at low altitude (around 900hPa) is also observed
 304 between 16°N and 18°N for AEW_{S3-5day}. These features are consistent with two AEWs regimes described
 305 by Wu et al. (2013). Around 10°N, the West African westerly jet (WAWJ) is visible, with mean winds
 306 reaching 3 m/s in ERA5 and about 5 m/s in the coupled model. It extends from the surface to 800hPa,
 307 and is known to be the supplier of moisture from the ocean to the West African rain system (Lamb,

308 1983; Grist and Nicholson, 2001; Liu et al., 2020). The 3–5 day filtering (Figure 5e) eliminates the low-
 309 frequency background circulation associated with the WAWJ, which indicates that the variability mainly
 310 reflects transient synoptic disturbances consistent with the documented signature of AEWs. However,
 311 interactions between AEWs and the WAWJ cannot be ruled out. AEW-related anomalies can locally
 312 and temporarily modulate low-level westerly winds, leading to apparent spatial overlap between the
 313 WAWJ region and the AEW signal in surface wind diagnostics. This AEW-WAWJ coupling and its
 314 influence on low-level convergence and moisture transport have been addressed in previous studies
 315 (e.g., Hsieh and Cook, 2007; Leroux and Hall, 2009). Nevertheless, we interpret Figure 5e primarily as
 316 the surface footprint of AEW_{S3-5day}.

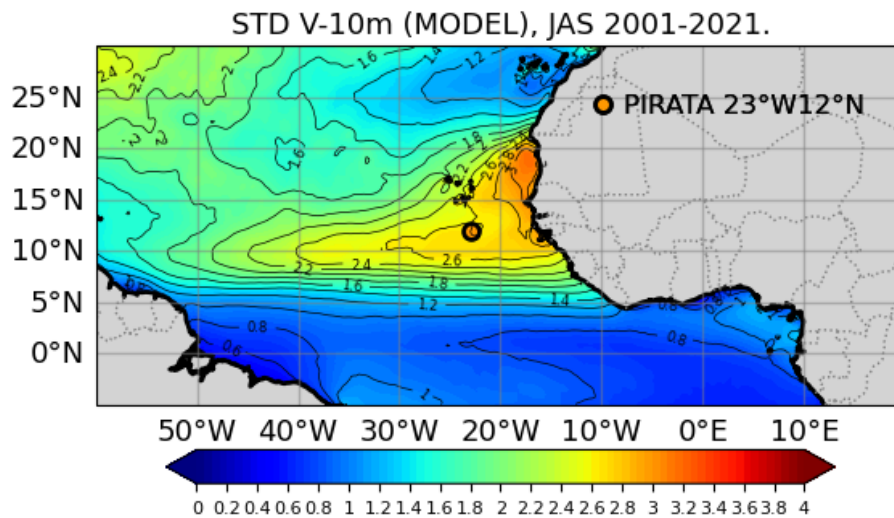
317 Overall, this comparison between the coupled model and atmospheric and oceanic datasets provides
 318 strong confidence in the model’s ability to represent the main characteristics of AEWs and SST
 319 variability. It also suggests that the 3–5-day band concentrates most of the surface wind variability,
 320 indicating AEW_{S3-5day} are expected to exert the strongest influence on surface processes and SST
 321 variability.



322
 323 **Figure 5: Latitudinal section of the standard deviation of meridional wind anomalies, longitudinally**
 324 **averaged between 25°W and 15°W, during JAS over the 2001–2021 period for (a), (b), (c) ERA5 and (d),**
 325 **(e), (f) the coupled model. Anomalies are band-pass filtered in the 2–10-day (left panels), 3–5-day (middle**
 326 **panels), and 6–9-day (right panels) ranges. Mean zonal winds are shown as contours to highlight the zonal**
 327 **jets.**

328 4 Ocean surface response to AEWs

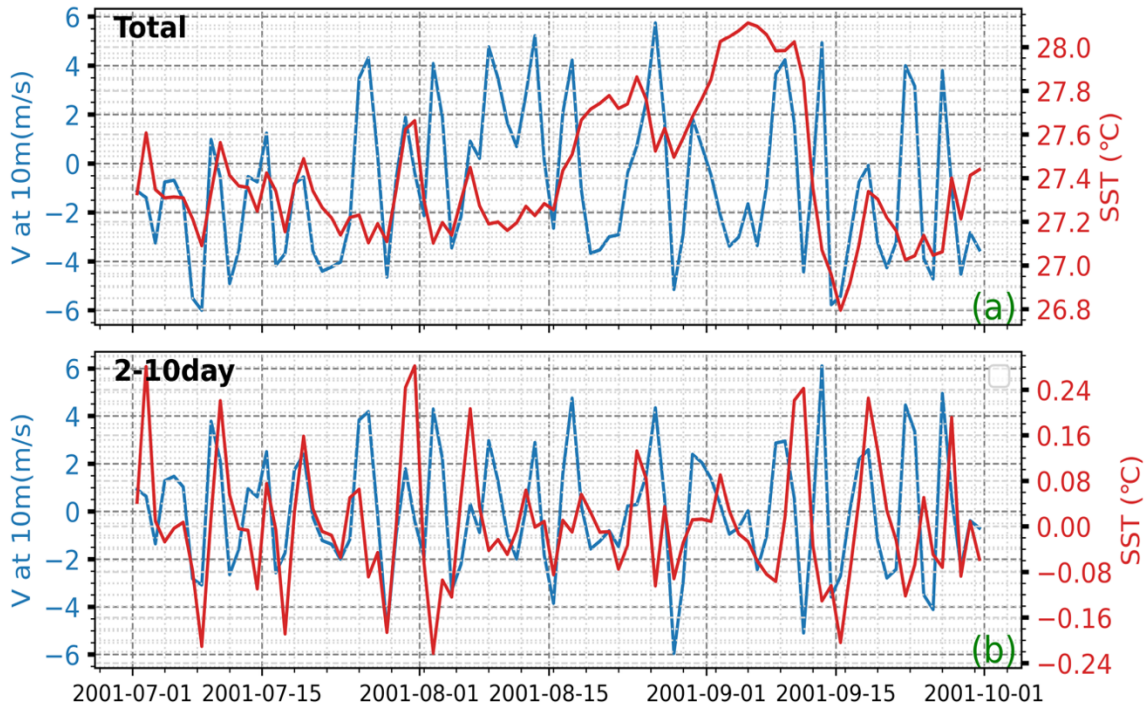
329 4.1 An index representative of AEWs



330

331 **Figure 6: Standard deviation of the 10-m meridional wind anomalies (V-10m), band-pass filtered in the 2–**
332 **10-day range, during the JAS period from 2001 to 2021 for the coupled model. The location of the PIRATA**
333 **mooring at 23°W-12°N is indicated with a black circle. It lies within the area of maximum variability.**

334 The colocalization of high wind and SST variability bands near 10°N (Fig. 1, Fig. 3), together with the
335 peak variability observed during JAS, strongly suggest a link between AEWs and the high-frequency
336 variability of SSTs. The influence of AEWs on the ocean surface of the TNA is assessed by projecting
337 the anomalies of relevant physical fields onto an index designed to be representative of AEWs activity.
338 In many previous studies, this index has been derived from the characteristic fields at the heart of these
339 disturbances, such as meridional wind, relative vorticity, or outgoing longwave radiation (OLR), and
340 has been applied to atmospheric variables (Diedhiou et al., 2001; Fink and Reiner, 2003; Jiang et al.,
341 2023; Kiladis et al., 2006). Given our focus on the impact of AEWs on SST, and the distinctive surface
342 signature of AEWs (Fig. 5), we have selected a 10-m surface wind index corresponding to the mean
343 meridional wind filtered over the 2-10-day period. The reference point for this index is set at the
344 PIRATA mooring located at 23°W -12°N—an area of strong variability, sufficiently offshore to avoid
345 coastal effects (Fig. 6). This site is therefore representative of the region of high surface wind variability
346 associated with the AEWs. Note that sensitivity tests carried out with other index sites, notably the one
347 located at 17.5°W-15°N proposed by Kiladis et al. (2006), indicate that, despite small variations in local
348 amplitude and statistical significance of the regressions, the large-scale spatial structures and physical
349 interpretation remain similar (not shown).



350

351 **Figure 7: SST (in red) and 10-m meridional wind velocity (in blue) at 23°W-12°N during JAS 2001 for the**
 352 **coupled model: (a) non-filtered data, (b) band-pass filtered in the 2–10-day range.**

353 To illustrate the relationship between SST and the 10-m meridional wind at a single location (at 23°W-
 354 12°N), Figure 7 shows their evolution during the boreal summer of 2001, together with the
 355 corresponding synoptic anomalies. This year was chosen as an illustrative example of the relationship
 356 between these two parameters. The 10-m meridional wind alternates between southward (negative) and
 357 northward (positive) directions, as the area is located within the ITCZ during this period, resulting in
 358 fluctuations ranging from -6 m/s to 6 m/s.

359 The high-frequency peaks, although generally offset by about 1-2 days, show a notable degree of
 360 correspondence, particularly in July, when strong southward wind bursts are often associated with
 361 surface cooling (Fig. 7b).

362 The unfiltered time series (Fig. 7a) highlight the covariability at longer timescales, while the filtered
 363 signals (Fig. 7b) isolate the synoptic component. During the boreal summer, much of the variance in the
 364 meridional wind is concentrated at the synoptic scale, which explains the relatively small difference
 365 between the filtered and unfiltered wind signals. In contrast, SST incorporates atmospheric forcing over
 366 longer periods; bandpass filtering therefore eliminates a significant portion of low-frequency variability,
 367 resulting in more pronounced differences between filtered and unfiltered SST time series.

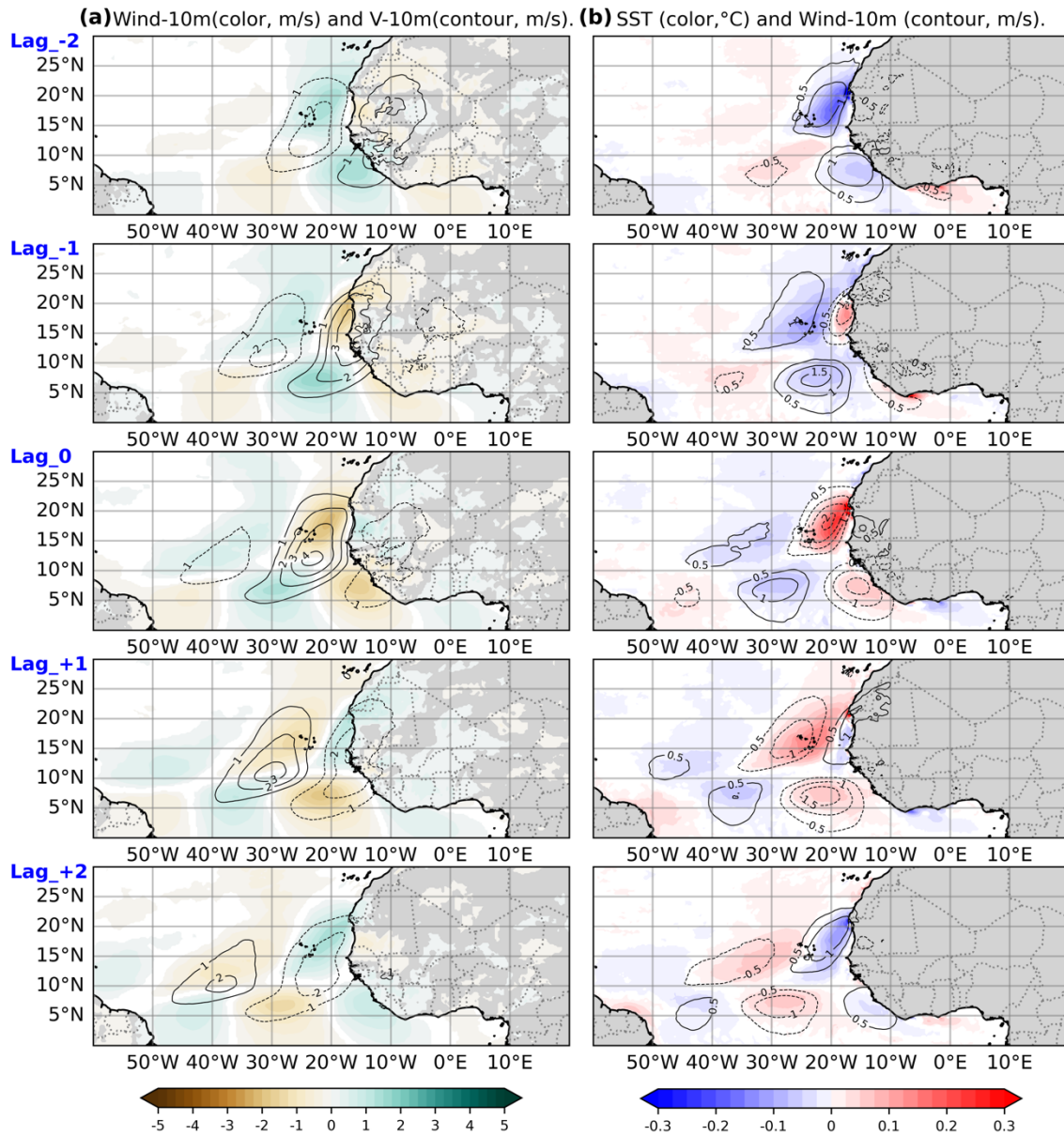
368 At synoptic timescales, the SST response to wind forcing is intermittent, characterized by variable time
 369 lags of about 1-2 days and a non-linear, integrative behavior, so that a strong pointwise linear
 370 correspondence is not expected. Nevertheless, several intense southward wind events, particularly in
 371 July, are followed by surface cooling, illustrating the influence of synoptic wind variability on SST.

372 Figure 7 is therefore intended as an illustrative example rather than a quantitative assessment of synoptic
373 air-sea coupling, which is addressed in the following sections using regression analyses.

374 **4.2 Signature of AEWs on the SST**

375 To investigate the impact of AEWs on SSTs, we performed a lagged linear regression analysis using
376 different model variables and the AEWs index, as defined in Section 4.1. The following results are
377 subject to a student's t-test, and only the statistically significant local fields (>95%) are shown.

378 Figure 8 shows the regression of the meridional winds at different time lags (in days), displaying the
379 evolution of patterns typical of AEWs. Southwest–northeast oriented structures, with a meridional
380 extent of 25–30° (about 3,000 km) and a zonal extent of 15°, propagate from east to west. They originate
381 from Central Africa with the lowest amplitude and spread towards West Africa. They reach a maximum
382 amplitude of more than 4 m/s over coastal regions at 15–20°, before gradually weakening as they
383 propagate westward into the central basin. This spatial and temporal behavior closely resembles that of
384 structures observed at higher altitudes (e.g., Hsieh and Cook, 2007; Thorncroft et al., 2008; Leroux and
385 Hall, 2009).



386

387 **Figure 8: Lagged regression of atmospheric and oceanic variables onto the 2–10-day AEWs index, defined**
 388 **as the 10-m meridional wind anomaly at 23°W-12°N (with a positive index corresponding to a northward**
 389 **wind anomaly). Left panels show 10-m wind speed anomalies (shading) and 10-m meridional wind**
 390 **anomalies (contours). Right panels show SST anomalies (shading) and 10-m wind speed anomalies (contours).**
 391 **Regressions are presented at different time lags (in days) to capture the temporal evolution associated with**
 392 **AEWs passage. The AEWs index time series used here is illustrated in Figure 7.**

393 As they propagate westward, AEWs structures associated with 2–10-day 10-m meridional wind
 394 anomalies exert opposite effects on the total surface wind field on either side of the Intertropical
 395 Convergence Zone (ITCZ). Specifically, a positive meridional wind anomaly leads to a weakening of
 396 the total wind speed north of the ITCZ and a strengthening of the wind south of it (Fig. 8a). The SST
 397 anomalies regressed on the AEWs index exhibit coherent cooling and warming patterns that propagate
 398 westward in phase with AEW-related wind anomalies (Fig. 8b). Stronger surface winds are generally

399 associated with negative SST anomalies, while weaker winds correspond to positive SST anomalies.
 400 The mean amplitude of the AEW-related SST response is on the order of ± 0.3 °C. More pronounced
 401 local anomalies are observed during the most intense events, as identified by the sensitivity tests
 402 described in Section 2.3, with amplitudes that can exceed ± 0.5 °C. AEWs play thus an important role in
 403 modulating SST variability in the tropical North Atlantic through surface wind forcing.

404 **5 The ocean mixed layer heat balance**

405 To better characterize the mechanisms through which the AEWs modulate SST in the TNA, we analyze
 406 the heat budget of the oceanic mixed layer (Jouanno et al., 2011a). This approach is particularly well-
 407 suited for isolating and quantifying the physical processes that drive temperature changes in the surface
 408 layer, including air-sea heat exchanges, horizontal advection, and vertical diffusion. All terms of the
 409 heat budget are calculated online in the coupled model. The temperature evolution in the surface layer,
 410 for a layer of thickness h , can be expressed as follows:

$$411 \quad \partial_t T = -\langle u \partial_x T \rangle_h - \langle v \partial_y T \rangle_h - \langle w \partial_z T \rangle_h + \langle D_t \rangle_h + \frac{(K_z \partial_z T)_{z=-h}}{h} + \frac{Q_s(1 - F_{-h}) + Q_{ns}}{\rho_0 C_p h}$$

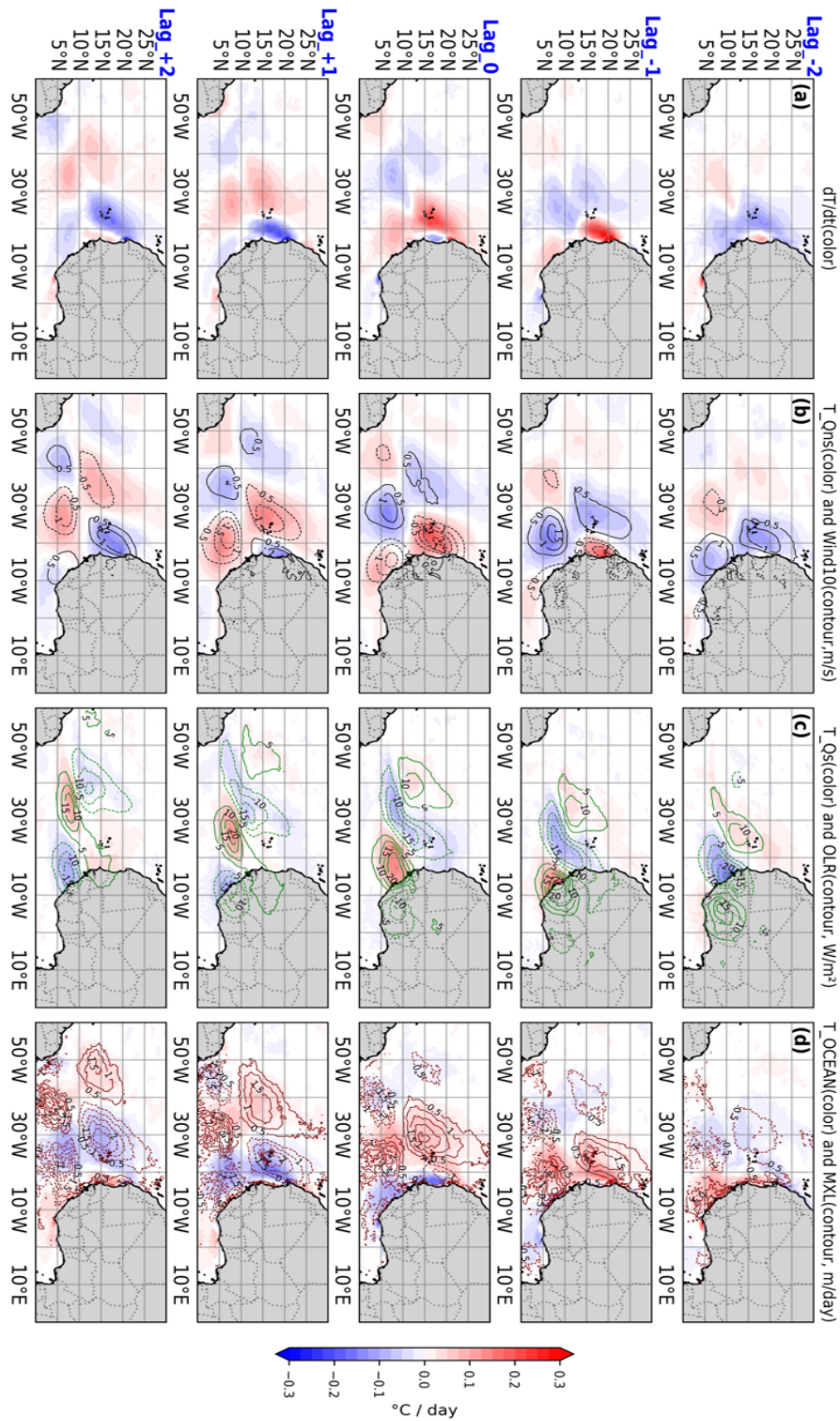
412 Here, T represents temperature; u , v , and w correspond to the zonal, meridional, and vertical currents,
 413 respectively; $\langle * \rangle_h$, the vertical averaging over the surface layer of thickness h . D_t represents lateral
 414 diffusive processes, and K_z is the vertical diffusivity evaluated at the base of the surface layer. The terms
 415 Q_s and Q_{ns} correspond to the net shortwave and non-solar surface heat fluxes, respectively, Q_{ns} including
 416 net longwave radiation as well as sensible and latent heat fluxes. The constant ρ_0 is the reference
 417 seawater density, and C_p is the specific heat capacity of seawater. F_{-h} denotes the fraction of shortwave
 418 radiation that penetrates to depth h . In this study, h is set to 5 m to ensure that the integrated trends
 419 remain consistent with near-surface ocean conditions.

420 Overall, the equation expresses temperature evolution as the sum of contributions from horizontal and
 421 vertical advection, lateral and vertical diffusion, and atmospheric forcing through Q_s and Q_{ns} . Terms
 422 associated to oceanic processes (advection and diffusion) are grouped under T_OCEAN , while
 423 atmospheric terms are separated into non-solar surface fluxes (T_Q_{ns}) and the shortwave component
 424 (T_Q_s).

425 **5.1 Oceanic processes versus heat fluxes in AEW-induced SST evolution**

426 As with SST, the different terms were time-filtered within the 2–10-day range prior to performing the
 427 regressions. Regressions were computed for the JAS period at time lags ranging from two days prior to
 428 two days after the AEW index, enabling us to track the evolution of each term during an AEW passage.
 429 For comparison, lagged regressions of 10 m wind speed, outgoing longwave radiation (OLR) and mixed
 430 layer depth are also superimposed. Note that OLR is used here as an indicator of convective activity
 431 associated with AEWs.

432 Figure 9 shows the regressions of the total temperature tendency and the different heat budget terms on
433 the AEW index. As noted earlier, the impact of AEWs on SST is strongest in coastal regions, where
434 their signature is most pronounced, and gradually weakens as they propagate offshore (Fig. 9a). At zero
435 lag, the regression shows warming around 23°W – 12°N , corresponding to a northward wind anomaly at
436 the index location and a negative total wind speed anomaly. The evolution of SST associated with AEWs
437 appears to result from multiple processes acting together. All of these processes contribute significantly
438 to temperature changes, with none being negligible, and their effects are not perfectly in phase. Term
439 $T_{Q_{ns}}$ (Fig. 9b) exhibits patterns resembling the overall temperature tendency but opposite to the wind
440 anomalies, which can be explained by the fact that increased wind speed enhances latent heat flux (not
441 shown), leading to SST cooling. Although weaker, solar radiation also contributes to the overall trend,
442 which is linked to the modulation of cloud cover (OLR, contours in Fig. 9c). For example, a cooling rate
443 of $-0.2^{\circ}\text{C}/\text{day}$ for T_{Q_s} corresponds to an OLR minimum of $-20 \text{ W}/\text{m}^2$, and vice versa. Interestingly,
444 these contributions are out of phase with $T_{Q_{ns}}$, with the largest effects occurring north of 10°N , near
445 the ITCZ during JAS.



446

447 **Figure 9: Lagged evolution of anomalies in the upper 5m ocean heat budget terms, regressed onto the 2–10-**
 448 **day AEWs index. Panels show: (column a) mixed-layer temperature tendency (dT/dt), (b) contribution from**
 449 **non-solar surface heat fluxes (T_{Qns} , shading) with 10-m wind speed anomalies overlaid (contours), (c)**
 450 **contribution from solar radiation (T_{Qs} , shading) with OLR anomalies (contours), and (d) oceanic**
 451 **processes (T_{OCEAN} , shading) with mixed-layer depth (MXL) anomalies (contours). Regressions are**
 452 **presented at different time lags (in days) to capture the temporal evolution associated with AEWs passage.**

453 The contribution of oceanic processes to SST modulation represents a key part of the ocean's response
454 to AEWs (Fig. 9d). Note that thermal advection is negligible offshore and very weak near some coastal
455 areas. Vertical mixing (vertical diffusion) primarily controls T_OCEAN (not shown). The observed
456 cooling and warming patterns correspond, respectively, to positive (deepening) and negative
457 (shallowing) mixed layer depth anomalies of approximately ± 2 m.

458 The temporal evolution at different lags indicates that the cooling induced by T_OCEAN is associated
459 with increasing wind speeds (Fig. 9b), indicating that the two signals (wind and T_OCEAN) are in phase
460 quadrature. This indicates that the intensified winds associated with AEWs deepen the mixed layer,
461 entraining cooler subsurface water to the surface and thereby cooling the SST. At zero lag, T_Qns
462 cooling rates reach approximately -0.2 °C/day, while T_OCEAN (mainly vertical mixing, not shown)
463 accounts for up to -0.15 °C/day, confirming that both mechanisms contribute with comparable
464 magnitudes. This oceanic contribution refers to the T_OCEAN term; the predominance of vertical
465 mixing is inferred from model diagnostics and is not explicitly displayed here. Thus, the SST response
466 to AEWs results from a complex interplay between the effects of local wind speed on air-sea fluxes, the
467 modulation of solar radiation by cloud cover, and the mixed layer deepening during phases of wind
468 fluctuations.

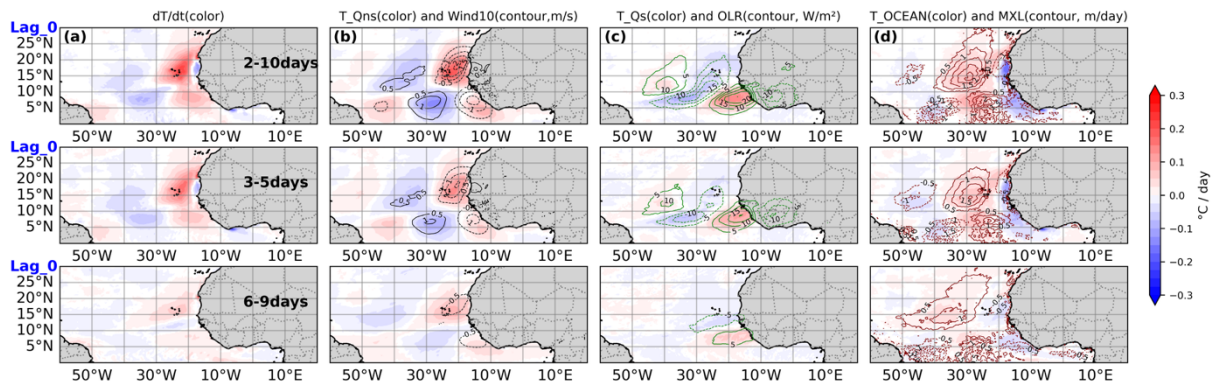
469 Previous observational studies of the heat balance of the mixing layer, such as [Foltz et al. \(2003\)](#) and
470 [Hummels et al. \(2014\)](#), have focused primarily on seasonal to interannual variability, rather than
471 synoptic time scales. Therefore, to our knowledge, there is currently no direct observational reference
472 documenting the decomposition of temperature trends in the mixing layer at synoptic time scales.

473 Nevertheless, these studies highlight the important role of vertical mixing in regulating surface
474 temperature variability under the effect of increased wind forcing. In addition, the seasonal heat balance
475 from this model has already been discussed in [Gévaudan et al. \(2021\)](#) and previously in a series of
476 studies ([Jouanno et al., 2011a, b](#)), all of which emphasize the important role of vertical mixing in this
477 balance. The synoptic results presented here are therefore consistent with previous seasonal assessments,
478 while extending the analysis to higher frequency variability.

479 **5.2 Dissociating the impact of AEWs in the 3-5 and 6-9-day bands**

480 As discussed previously, AEWs occur over two distinct time scales, typically corresponding to the 3–5-
481 day and 6–9-day bands, which have different meridional distributions. Consequently, the regression
482 results presented earlier may be biased toward the more dominant wave band. To determine whether
483 similar processes occur for both wave types, we perform regression analyses of dT/dt and its contributing
484 terms using indices filtered separately for each band (Figure 10). The results confirm that AEWs in the
485 3–5-day band have a significantly greater impact on SST compared to those in the 6–9-day band. This
486 is consistent with the surface signature of $AEW_{S3-5day}$ between $5^{\circ}N$ and $25^{\circ}N$, as opposed to the higher-
487 altitude and more northerly $AEW_{S6-9day}$ structures (Fig. 5).

488 As a result, 3-5-day waves more effectively force air-sea heat fluxes and mixing layer processes, leaving
 489 a clear imprint on SST. Although this behavior is physically expected given the respective wind
 490 structures, its quantitative expression in terms of SST response and contributions to the heat balance is
 491 not trivial a priori, due to the integrative and non-linear nature of the ocean mixed layer response. The
 492 comparison between the two frequency bands therefore clarifies the dynamic mechanisms by which
 493 AEWs influence the ocean surface. For both types of AEWs, the results indicate that the SST response
 494 arises from a combination of air-sea fluxes and vertical mixing, which contribute in comparable
 495 proportions, although the overall amplitude of the response is significantly weaker for the 6–9-day band.



496
 497 **Figure 10: Same as Figure 9, but shown at lag 0 only. Panels present anomalies in the surface layer**
 498 **temperature tendency (dT/dt) and its contributing terms for the 2–10-day (top panels), 3–5-day (middle**
 499 **panels), and 6–9-day bands (bottom panels).**

500 **6 Conclusion**

501 A 21-year regional coupled simulation over the tropical Atlantic is used to investigate the influence of
 502 African Easterly Waves on SST in the TNA and to quantitatively assess the underlying processes.
 503 Although small biases in SST and wind are present, comparisons with reference satellite observations
 504 and atmospheric reanalysis datasets demonstrate that the simulation provides a robust framework and a
 505 solid tool for studying ocean–atmosphere interactions in the tropical Atlantic. The characteristics of
 506 AEWs—represented by westward-propagating meridional wind anomalies between 5°N and 25°N, with
 507 a typical zonal wavelength of about 15°—are well captured by the simulation and show good agreement
 508 with observations and reanalysis datasets. In addition, the temporal separation into 3–5-day and 6–9-
 509 day variability reveals distinct branches characterized by their latitude and vertical structure, in
 510 agreement with the literature.

511 This study highlights for the first time a robust and consistent AEW-related imprint on SST in the
 512 tropical Atlantic, with anomalies of approximately $\pm 0.3^{\circ}\text{C}$ on average, increasing to approximately ± 0.5
 513 $^{\circ}\text{C}$ for the of approximately $\pm 0.3^{\circ}\text{C}$ on average, increasing to approximately stronger events. The
 514 combined effect of latent heat fluxes, shortwave radiation, and vertical mixing underscores the critical
 515 role of AEWs in shaping mixed-layer dynamics.

516 The signature of AEWs on SST is identified by regressing SST anomalies and temperature tendency
517 terms onto filtered wind anomalies — used as a representative AEW index — onto SST fields, revealing
518 a significant and consistent AEW-related imprint. A similar projection applied to the temperature
519 tendency terms of the heat budget shows that AEW-related SST anomalies result from a combination of
520 non-solar heat flux fluctuations (mainly latent) driven by surface winds, shortwave radiation variations
521 linked to cloud cover changes, and modulation of ocean mixing associated with mixed-layer variability.
522 The results also highlight a stronger SST response between 5°N and 20°N from 3–5-day AEWs
523 compared to 6–9-day AEWs, consistent with their more pronounced surface signal south of 20°–25°N.
524 While such methodologies have been applied to atmospheric fields, to our knowledge, this is the first
525 time that this type of identification has been demonstrated for oceanic fields.

526 This quantitative assessment of the impact of African Easterly Waves (AEWs) on dynamic and
527 thermodynamic heat fluxes is useful when compared with previous studies. Several studies have shown
528 that the role of atmospheric wind and latent heat fluxes dominates variability from intraseasonal to
529 interdecadal timescales (Foltz et al., 2003), while the role of mixing has mainly been identified as
530 enhancing in the upper thermocline within 2°N–2°S (Jouanno et al., 2011a) relative to off-equatorial
531 regions (Hummels et al., 2014). However, turbulence remains the most challenging component to
532 quantify and assess, and high-frequency phenomena can also contribute to local mixing outside the
533 equatorial region (Foltz et al., 2020; Hummels et al., 2020). Although this mechanism is not explicitly
534 diagnosed here, the mixing component is consistent with a possible influence of near-inertial motions,
535 which have been shown to enhance upper-ocean mixing in previous studies over extensive regions of
536 the eastern TNA (D’Asaro, 1985; Plueddemann and Farrar, 2006; Hummels et al., 2020). Further
537 investigation is therefore required to quantify the role of near-inertial activity in the mixing contribution

538 This raises questions about our methodology, which relies on regressing SST and heat-budget terms
539 onto a wind-based AEW index. While this approach primarily captures synchronous responses, it may
540 overlook effects that occur out of phase. Tests applying time lags from –2 to +2 days did not significantly
541 change the results. This indicates that, unlike the more immediate effects of solar radiation and latent
542 heat fluxes linked to cloud cover and wind fluctuations, the influence of near-inertial waves—generated
543 by AEW-related wind bursts and potentially propagating over several days—may be underestimated.
544 This could be addressed through additional numerical experiments, such as masking AEWs by nudging
545 winds toward climatology, to better isolate oceanic processes and their influence on interannual
546 timescales.

547 Beyond advancing process understanding, these findings of this paper are relevant for improving the
548 representation of synoptic variability in coupled models, reducing persistent SST biases, and ultimately
549 enhancing tropical cyclone prediction and seasonal climate forecasts.

550 **Open research**

551 Temperature, salinity, wind and heat flux data from the PIRATA moorings used in this study are
552 available from the Global Tropical Moored Buoy Array at
553 <https://www.pmel.noaa.gov/tao/drupal/disdel/>. NOAA OI SST V2 High Resolution Dataset data
554 provided by the NOAA PSL, Boulder, Colorado, USA (<https://doi.org/10.1175/JCLI-D-20-0166.1>).
555 ERA5, ASCAT. Numerical simulated fields used for diagnostics are available at
556 (<https://doi.org/10.6084/m9.figshare.30095101>). All analyses were performed and all figures created
557 using Python.

558 **Author contributions**

559 MM: Investigation, Software, Visualization, Writing (original draft), Review and Editing (original
560 draft).

561 FG: Project administration, Supervision, Validation, Writing (original draft), Review and Editing
562 (original draft).

563 MG: Software, Validation, Writing (original draft), Review and Editing (original draft).

564 MD: Review and Editing (original draft).

565 IS: Review and Editing (original draft).

566 JJ: Supervision, Validation, Writing (original draft), Review and Editing (original draft).

567 **Acknowledgments**

568 This work was supported by the French National program CNES TOSCA NICITA project. M.M. is
569 funded by the French National Research Institute for Sustainable Development (IRD) through an ARTS
570 grant. Computing resources were provided by DARI under grant GEN7298. The authors also
571 acknowledge the GTMBA Project Office of NOAA/PMEL and the PIRATA program for freely
572 providing data from the tropical Atlantic buoy array.

573

574 **References**

- 575 Banzon, V., Smith, T. M., Chin, T. M., Liu, C., and Hankins, W.: A long-term record of blended satellite and in
576 situ sea-surface temperature for climate monitoring, modeling and environmental studies, *Earth System Science*
577 *Data*, 8, 165–176, <https://doi.org/10.5194/essd-8-165-2016>, 2016.
- 578 Bercos-Hickey, E. and Patricola, C. M.: Drivers of Atlantic Tropical Cyclogenesis: African Easterly Waves and
579 the Environment, *Geophysical Research Letters*, 52, e2024GL112002,
580 <https://doi.org/https://doi.org/10.1029/2024GL112002>, 2025.
- 581 Bercos-Hickey, E., Nathan, T. R., and Chen, S.-H.: Saharan dust and the African easterly jet–African easterly
582 wave system: Structure, location and energetics, *Quarterly Journal of the Royal Meteorological Society*, 143,
583 2797–2808, <https://doi.org/https://doi.org/10.1002/qj.3128>, 2017.
- 584 Berry, G. J. and Thorncroft, C.: Case Study of an Intense African Easterly Wave, *Monthly Weather Review*, 133,
585 752–766, <https://doi.org/10.1175/MWR2884.1>, 2005.
- 586 Bourlès, B., Araujo, M., McPhaden, M. J., Brandt, P., Foltz, G. R., Lumpkin, R., Giordani, H., Hernandez, F.,
587 Lefèvre, N., Nobre, P., Campos, E., Saravanan, R., Trotte-Duhà, J., Dengler, M., Hahn, J., Hummels, R.,
588 Lübbecke, J. F., Rouault, M., Cotrim, L., Sutton, A., Jochum, M., and Perez, R. C.: PIRATA: A Sustained
589 Observing System for Tropical Atlantic Climate Research and Forecasting, *Earth and Space Science*, 6, 577–616,
590 <https://doi.org/https://doi.org/10.1029/2018EA000428>, 2019.
- 591 Burpee, R. W.: *The Origin and Structure of Easterly Waves in the Lower Troposphere of North Africa*, 1972.
- 592 Carlson, T. N.: *SOME REMARKS ON AFRICAN DISTURBANCES AND THEIR PROGRESS OVER THE*
593 *TROPICAL ATLANTIC*, 1969.
- 594 Craig, A., Valcke, S., and Coquart, L.: Development and performance of a new version of the OASIS coupler,
595 OASIS3-MCT_3.0, *Geoscientific Model Development*, 10, 3297–3308, [https://doi.org/10.5194/gmd-10-3297-](https://doi.org/10.5194/gmd-10-3297-2017)
596 2017, 2017.
- 597 Cromwell, T.: *Circulation in a meridional plane in the central equatorial Pacific*, 1953.
- 598 Danso, D. K., Patricola, C. M., and Bercos-Hickey, E.: Influence of African Easterly Wave Suppression on Atlantic
599 Tropical Cyclone Activity in a Convection-Permitting Model, *Geophysical Research Letters*, 49, e2022GL100590,
600 <https://doi.org/https://doi.org/10.1029/2022GL100590>, 2022.
- 601 D’Asaro, E. A.: The energy flux from the wind to near-inertial motions in the surface mixed layer, *Journal of*
602 *Physical Oceanography*, 15, 1043–1059, 1985.
- 603 Deppenmeier, A.-L., Haarsma, R. J., Heerwaarden, C. van, and Hazeleger, W.: The Southeastern Tropical Atlantic
604 SST Bias Investigated with a Coupled Atmosphere–Ocean Single-Column Model at a PIRATA Mooring Site,
605 *Journal of Climate*, 33, 6255–6271, <https://doi.org/10.1175/JCLI-D-19-0608.1>, 2020.
- 606 Diedhiou, A., Janicot, S., Viltard, A., De Felice, P., and Laurent, H.: A fast moving easterly wave of the West
607 Africa troposphere, *Meteorology and Atmospheric Physics*, 69, 39–47, 1998a.
- 608 Diedhiou, A., Janicot, S., Viltard, A., and de Felice, P.: Evidence of two regimes of easterly waves over West
609 Africa and the tropical Atlantic, *Geophysical Research Letters*, 25, 2805–2808, 1998b.
- 610 Diedhiou, A., Janicot, S., Viltard, A., de Felice, P., and Laurent, H.: Easterly wave regimes and associated
611 convection over West Africa and tropical Atlantic: results from the NCEP/NCAR and ECMWF reanalyses,
612 *Climate Dynamics*, 15, 795–822, <https://doi.org/10.1007/s003820050316>, 1999.
- 613 Diedhiou, A., Janicot, S., Viltard, A., and de Félice, P.: Composite patterns of easterly disturbances over West
614 Africa and the tropical Atlantic: a climatology from the 1979–95 NCEP/NCAR reanalyses, *Climate Dynamics*,
615 18, 241–253, <https://doi.org/10.1007/s003820100173>, 2001.

- 616 Diedhiou, A., Machado, L. A. T., and Laurent, H.: Mean kinematic characteristics of synoptic easterly disturbances
617 over the Atlantic, *Adv. Atmos. Sci.*, 27, 483–499, <https://doi.org/10.1007/s00376-009-9092-5>, 2010.
- 618 Donlon, C. J., Minnett, P. J., Gentemann, C., Nightingale, T. J., Barton, I. J., Ward, B., and Murray, M. J.: Toward
619 Improved Validation of Satellite Sea Surface Skin Temperature Measurements for Climate Research, *Journal of*
620 *Climate*, 15, 353–369, [https://doi.org/10.1175/1520-0442\(2002\)015%3C0353:TIVOSS%3E2.0.CO;2](https://doi.org/10.1175/1520-0442(2002)015%3C0353:TIVOSS%3E2.0.CO;2), 2002.
- 621 Dunkerton, T. J., Montgomery, M., and Wang, Z.: Tropical cyclogenesis in a tropical wave critical layer: Easterly
622 waves, *Atmospheric Chemistry and Physics*, 9, 5587–5646, 2009.
- 623 Emanuel, K.: Increasing destructiveness of tropical cyclones over the past 30 years, *Nature*, 436, 686–688,
624 <https://doi.org/10.1038/nature03906>, 2005.
- 625 Enfield, D. B. and Lee, S.: The Heat Balance of the Western Hemisphere Warm Pool, *Journal of Climate*, 18,
626 2662–2681, <https://doi.org/10.1175/JCLI3427.1>, 2005.
- 627 Felice, P. D., Monkam, D., Viltard, A., and Ouss, C.: Characteristics of North African 6–9 Day Waves during
628 Summer 1981, *Monthly Weather Review*, 118, 2624–2633, [https://doi.org/10.1175/1520-0493\(1990\)118%3C2624:CONADW%3E2.0.CO;2](https://doi.org/10.1175/1520-0493(1990)118%3C2624:CONADW%3E2.0.CO;2), 1990.
- 630 Felice, P. de, Viltard, A., and Oubuih, J.: A Synoptic-Scale Wave of 6–9-Day Period in the Atlantic Tropical
631 Troposphere during Summer 1981, *Monthly Weather Review*, 121, 1291–1298, [https://doi.org/10.1175/1520-0493\(1993\)121%3C1291:ASSWOD%3E2.0.CO;2](https://doi.org/10.1175/1520-0493(1993)121%3C1291:ASSWOD%3E2.0.CO;2), 1993.
- 633 Ferry, N., Parent, L., Garric, G., Bricaud, C., Testut, C., Le Galloudec, O., Lellouche, J., Drevillon, M., Greiner,
634 E., and Barnier, B.: GLORYS2V1 global ocean reanalysis of the altimetric era (1992–2009) at meso scale,
635 *Mercator Ocean–Quarterly Newsletter*, 44, 2012.
- 636 Fink, A. H. and Reiner, A.: Spatio-temporal variability of the relation between African easterly waves and West
637 African squall lines in 1998 and 1999., , 108, 2003.
- 638 Foltz, G. R., Grodsky, S. A., Carton, J. A., and McPhaden, M. J.: Seasonal mixed layer heat budget of the tropical
639 Atlantic Ocean, *Journal of Geophysical Research: Oceans*, 108,
640 <https://doi.org/https://doi.org/10.1029/2002JC001584>, 2003.
- 641 Foltz, G. R., Hummels, R., Dengler, M., Perez, R. C., and Araujo, M.: Vertical Turbulent Cooling of the Mixed
642 Layer in the Atlantic ITCZ and Trade Wind Regions, *Journal of Geophysical Research: Oceans*, 125,
643 e2019JC015529, <https://doi.org/https://doi.org/10.1029/2019JC015529>, 2020.
- 644 Garnesson, P., Mangin, A., Fanton d’Andon, O., Demaria, J., and Bretagnon, M.: The CMEMS GlobColour
645 chlorophyll a product based on satellite observation: multi-sensor merging and flagging strategies, *Ocean Science*,
646 15, 819–830, <https://doi.org/10.5194/os-15-819-2019>, 2019.
- 647 Gévaudan, M., Jouanno, J., Durand, F., Morvan, G., Renault, L., and Samson, G.: Influence of ocean salinity
648 stratification on the tropical Atlantic Ocean surface, *Clim Dyn*, 57, 321–340, <https://doi.org/10.1007/s00382-021-05713-z>, 2021.
- 650 Gévaudan, M., Durand, F., and Jouanno, J.: Influence of the Amazon-Orinoco Discharge Interannual Variability
651 on the Western Tropical Atlantic Salinity and Temperature, *Journal of Geophysical Research: Oceans*, 127,
652 e2022JC018495, <https://doi.org/https://doi.org/10.1029/2022JC018495>, 2022.
- 653 Gill, A. E.: Some simple solutions for heat-induced tropical circulation, *Quarterly Journal of the Royal*
654 *Meteorological Society*, 106, 447–462, <https://doi.org/https://doi.org/10.1002/qj.49710644905>, 1980.
- 655 Graham, N. E. and Barnett, T. P.: Sea Surface Temperature, Surface Wind Divergence, and Convection over
656 Tropical Oceans, *Science*, 238, 657–659, <https://doi.org/10.1126/science.238.4827.657>, 1987.
- 657 Grist, J. P.: Easterly Waves over Africa. Part I: The Seasonal Cycle and Contrasts between Wet and Dry Years,
658 *Monthly Weather Review*, 130, 197–211, [https://doi.org/10.1175/1520-0493\(2002\)130%3C0197:EWOAPI%3E2.0.CO;2](https://doi.org/10.1175/1520-0493(2002)130%3C0197:EWOAPI%3E2.0.CO;2), 2002.

- 660 Grist, J. P. and Nicholson, S. E.: A Study of the Dynamic Factors Influencing the Rainfall Variability in the West
661 African Sahel, *Journal of Climate*, 14, 1337–1359, [https://doi.org/10.1175/1520-0442\(2001\)014%3C1337:ASOTDF%3E2.0.CO;2](https://doi.org/10.1175/1520-0442(2001)014%3C1337:ASOTDF%3E2.0.CO;2), 2001.
- 663 Hastenrath, S. and Greischar, L.: Circulation mechanisms related to northeast Brazil rainfall anomalies, *Journal of Geophysical Research: Atmospheres*, 98, 5093–5102, <https://doi.org/https://doi.org/10.1029/92JD02646>, 1993.
- 665 Hersbach, H., Bell, B., Berrisford, P., Hirahara, S., Horányi, A., Muñoz-Sabater, J., Nicolas, J., Peubey, C., Radu, R., and Schepers, D.: The ERA5 global reanalysis, *Quarterly Journal of the Royal Meteorological Society*, 146, 1999–2049, 2020.
- 668 Hsieh, J.-S. and Cook, K. H.: A Study of the Energetics of African Easterly Waves Using a Regional Climate Model, *Journal of the Atmospheric Sciences*, 64, 421–440, <https://doi.org/10.1175/JAS3851.1>, 2007.
- 670 Hummels, R., Dengler, M., Brandt, P., and Schlundt, M.: Diapycnal heat flux and mixed layer heat budget within the Atlantic Cold Tongue, *Climate Dynamics*, 43, 3179–3199, <https://doi.org/10.1007/s00382-014-2339-6>, 2014.
- 672 Hummels, R., Dengler, M., Rath, W., Foltz, G. R., Schütte, F., Fischer, T., and Brandt, P.: Surface cooling caused by rare but intense near-inertial wave induced mixing in the tropical Atlantic, *Nature Communications*, 11, 3829, <https://doi.org/10.1038/s41467-020-17601-x>, 2020.
- 675 J. Figa-Saldaña, M. R. D., J. J. W. Wilson, E. Attema, R. Gelsthorpe and Stoffelen, A.: The advanced scatterometer (ASCAT) on the meteorological operational (MetOp) platform: A follow on for European wind scatterometers, *Canadian Journal of Remote Sensing*, 28, 404–412, <https://doi.org/10.5589/m02-035>, 2002.
- 678 Janiga, M. A. and Thorncroft, C. D.: Regional differences in the kinematic and thermodynamic structure of African easterly waves, *Quarterly Journal of the Royal Meteorological Society*, 139, 1598–1614, <https://doi.org/https://doi.org/10.1002/qj.2047>, 2013.
- 681 Jiang, X., Su, H., Chen, S. S., and Ullrich, P. A.: Simulation of African Easterly Waves in a Global Climate Model, *Journal of Climate*, 36, 1415–1433, <https://doi.org/10.1175/JCLI-D-22-0090.1>, 2023.
- 683 Jonville, T., Flamant, C., and Lavaysse, C.: Dynamical study of three African easterly waves in September 2021, *Quarterly Journal of the Royal Meteorological Society*, 150, 2489–2509, 2024.
- 685 Jonville, T., Cornillault, E., Lavaysse, C., Peyrillé, P., and Flamant, C.: Distinguishing north and south African Easterly Waves with a spectral method: Implication for tropical cyclogenesis from mergers in the North Atlantic, *Quarterly Journal of the Royal Meteorological Society*, 151, e4909, <https://doi.org/https://doi.org/10.1002/qj.4909>, 2025.
- 689 Jouanno, J., Marin, F., du Penhoat, Y., Sheinbaum, J., and Molines, J.-M.: Seasonal heat balance in the upper 100 m of the equatorial Atlantic Ocean, *Journal of Geophysical Research: Oceans*, 116, <https://doi.org/https://doi.org/10.1029/2010JC006912>, 2011a.
- 692 Jouanno, J., Marin, F., Penhoat, Y. du, Molines, J. M., and Sheinbaum, J.: Seasonal Modes of Surface Cooling in the Gulf of Guinea, *Journal of Physical Oceanography*, 41, 1408–1416, <https://doi.org/10.1175/JPO-D-11-031.1>, 2011b.
- 695 Kiladis, G. N., Thorncroft, C. D., and Hall, N. M. J.: Three-Dimensional Structure and Dynamics of African Easterly Waves. Part I: Observations, *Journal of the Atmospheric Sciences*, 63, 2212–2230, <https://doi.org/10.1175/JAS3741.1>, 2006.
- 698 Lamb, P. J.: Sub-saharan rainfall update for 1982; continued drought, *Journal of climatology*, 3, 419–422, 1983.
- 699 Leroux, S. and Hall, N. M. J.: On the Relationship between African Easterly Waves and the African Easterly Jet, *Journal of the Atmospheric Sciences*, 66, 2303–2316, <https://doi.org/10.1175/2009JAS2988.1>, 2009.
- 701 Liu, W., Cook, K. H., and Vizy, E. K.: Role of the West African westerly jet in the seasonal and diurnal cycles of precipitation over West Africa, *Climate Dynamics*, 54, 843–861, <https://doi.org/10.1007/s00382-019-05035-1>, 2020.

- 704 Madec, G., Bell, M., Blaker, A., Bricaud, C., Bruciaferri, D., Castrillo, M., Calvert, D., Chanut, J., Clementi, E.,
705 Coward, A., Epicoco, I., Éthé, C., Ganderton, J., Harle, J., Hutchinson, K., Iovino, D., Lea, D., Lovato, T., Martin,
706 M., Martin, N., Mele, F., Martins, D., Masson, S., Mathiot, P., Mele, F., Mocavero, S., Müller, S., Nurser, A. J.
707 G., Paronuzzi, S., Peltier, M., Person, R., Rousset, C., Rynders, S., Samson, G., Téchené, S., Vancoppenolle, M.,
708 and Wilson, C.: NEMO Ocean Engine Reference Manual, , <https://doi.org/10.5281/zenodo.8167700>, 2023.
- 709 Maritorena, S., d'Andon, O. H. F., Mangin, A., and Siegel, D. A.: Merged satellite ocean color data products using
710 a bio-optical model: Characteristics, benefits and issues, *Remote Sensing of Environment*, 114, 1791–1804,
711 <https://doi.org/https://doi.org/10.1016/j.rse.2010.04.002>, 2010.
- 712 Mekonnen, A., Thorncroft, C. D., and Aiyyer, A. R.: Analysis of Convection and Its Association with African
713 Easterly Waves, *Journal of Climate*, 19, 5405–5421, <https://doi.org/10.1175/JCLI3920.1>, 2006.
- 714 Mickett, J. B., Serra, Y. L., Cronin, M. F., and Alford, M. H.: Resonant Forcing of Mixed Layer Inertial Motions
715 by Atmospheric Easterly Waves in the Northeast Tropical Pacific, *Journal of Physical Oceanography*, 40, 401–
716 416, <https://doi.org/10.1175/2009JPO4276.1>, 2010.
- 717 Moura, A. D. and Shukla, J.: On the Dynamics of Droughts in Northeast Brazil: Observations, Theory and
718 Numerical Experiments with a General Circulation Model, *Journal of Atmospheric Sciences*, 38, 2653–2675,
719 [https://doi.org/10.1175/1520-0469\(1981\)038%3C2653:OTDODI%3E2.0.CO;2](https://doi.org/10.1175/1520-0469(1981)038%3C2653:OTDODI%3E2.0.CO;2), 1981.
- 720 Murray, M. J., Allen, M. R., Merchant, C. J., Harris, A. R., and Donlon, C. J.: Direct observations of skin-bulk
721 SST variability, *Geophysical Research Letters*, 27, 1171–1174,
722 <https://doi.org/https://doi.org/10.1029/1999GL011133>, 2000.
- 723 Nicholson, S. E.: A revised picture of the structure of the “monsoon” and land ITCZ over West Africa, *Climate*
724 *Dynamics*, 32, 1155–1171, <https://doi.org/10.1007/s00382-008-0514-3>, 2009.
- 725 Nobre, P. and Shukla, J.: Variations of Sea Surface Temperature, Wind Stress, and Rainfall over the Tropical
726 Atlantic and South America, *Journal of Climate*, 9, 2464–2479, [https://doi.org/10.1175/1520-0442\(1996\)009%3C2464:VOSSTW%3E2.0.CO;2](https://doi.org/10.1175/1520-0442(1996)009%3C2464:VOSSTW%3E2.0.CO;2), 1996.
- 728 Opoku-Ankomah, Y. and Cordery, I.: Atlantic Sea Surface Temperatures and Rainfall Variability in Ghana,
729 *Journal of Climate*, 7, 551–558, [https://doi.org/10.1175/1520-0442\(1994\)007%3C0551:ASSTAR%3E2.0.CO;2](https://doi.org/10.1175/1520-0442(1994)007%3C0551:ASSTAR%3E2.0.CO;2),
730 1994.
- 731 Plueddemann, A. J. and Farrar, J. T.: Observations and models of the energy flux from the wind to mixed-layer
732 inertial currents, *Deep Sea Research Part II: Topical Studies in Oceanography*, 53, 5–30,
733 <https://doi.org/https://doi.org/10.1016/j.dsr2.2005.10.017>, 2006.
- 734 Raj, J., Bangalath, H. K., and Stenchikov, G.: Future projection of the African easterly waves in a high-resolution
735 atmospheric general circulation model, *Climate Dynamics*, 61, 3081–3102, <https://doi.org/10.1007/s00382-023-06720-y>, 2023.
- 737 Reed, R. J., Klinker, E., and Hollingsworth, A.: The structure and characteristics of African easterly wave
738 disturbances as determined from the ECMWF operational analysis/forecast system, *Meteorology and Atmospheric*
739 *Physics*, 38, 22–33, <https://doi.org/10.1007/BF01029944>, 1988.
- 740 Reffray, G., Bourdalle-Badie, R., and Calone, C.: Modelling turbulent vertical mixing sensitivity using a 1-D
741 version of NEMO, *Geoscientific Model Development*, 8, 69–86, <https://doi.org/10.5194/gmd-8-69-2015>, 2015.
- 742 Reynolds, R. W., Smith, T. M., Liu, C., Chelton, D. B., Casey, K. S., and Schlax, M. G.: Daily High-Resolution-
743 Blended Analyses for Sea Surface Temperature, *Journal of Climate*, 20, 5473–5496,
744 <https://doi.org/10.1175/2007JCLI1824.1>, 2007.
- 745 Russell, J. O., Aiyyer, A., White, J. D., and Hannah, W.: Revisiting the connection between African Easterly
746 Waves and Atlantic tropical cyclogenesis, *Geophysical Research Letters*, 44, 587–595,
747 <https://doi.org/https://doi.org/10.1002/2016GL071236>, 2017.

- 748 Russell, J. O. H., Aiyyer, A., and Dylan White, J.: African Easterly Wave Dynamics in Convection-Permitting
749 Simulations: Rotational Stratiform Instability as a Conceptual Model, *Journal of Advances in Modeling Earth*
750 *Systems*, 12, e2019MS001706, <https://doi.org/https://doi.org/10.1029/2019MS001706>, 2020.
- 751 Semunegus, H., Mekonnen, A., and Schreck III, C. J.: Characterization of convective systems and their association
752 with African easterly waves, *International Journal of Climatology*, 37, 4486–4492,
753 <https://doi.org/https://doi.org/10.1002/joc.5085>, 2017.
- 754 Shi, Y., Huang, W., Wang, B., Yang, Z., He, X., and Qiu, T.: Origin of Warm SST Bias over the Atlantic Cold
755 Tongue in the Coupled Climate Model FGOALS-g2, *Atmosphere*, 9, <https://doi.org/10.3390/atmos9070275>, 2018.
- 756 Skamarock, C., Klemp, B., Dudhia, J., Gill, O., Liu, Z., Berner, J., Wang, W., Powers, G., Duda, G., Barker, D.
757 M., and Huang, X.: A Description of the Advanced Research WRF Model Version 4, 2019.
- 758 Skinner, C. B. and Diffenbaugh, N. S.: The contribution of African easterly waves to monsoon precipitation in the
759 CMIP3 ensemble, *Journal of Geophysical Research: Atmospheres*, 118, 3590–3609, 2013.
- 760 Stommel, H.: Wind-drift near the equator, *Deep Sea Research* (1953), 6, 298–302,
761 [https://doi.org/https://doi.org/10.1016/0146-6313\(59\)90088-7](https://doi.org/https://doi.org/10.1016/0146-6313(59)90088-7), 1959.
- 762 Sultan, B. and Janicot, S.: Abrupt shift of the ITCZ over West Africa and intra-seasonal variability, *Geophysical*
763 *Research Letters*, 27, 3353–3356, <https://doi.org/10.1029/1999GL011285>, 2000.
- 764 Sweet, W., Fett, R., Kerling, J., and Violette, P. L.: Air-Sea Interaction Effects in the Lower Troposphere Across
765 the North Wall of the Gulf Stream, *Monthly Weather Review*, 109, 1042–1052, [https://doi.org/10.1175/1520-0493\(1981\)109%3C1042:ASIEIT%3E2.0.CO;2](https://doi.org/10.1175/1520-0493(1981)109%3C1042:ASIEIT%3E2.0.CO;2), 1981.
- 767 Thompson, R. M., Payne, S. W., Recker, E. E., and Reed, R. J.: Structure and Properties of Synoptic-Scale Wave
768 Disturbances in the Intertropical Convergence Zone of the Eastern Atlantic, 1979.
- 769 Thorncroft, C. and Hodges, K.: African Easterly Wave Variability and Its Relationship to Atlantic Tropical
770 Cyclone Activity, *Journal of Climate*, 14, 1166–1179, [https://doi.org/10.1175/1520-0442\(2001\)014%3C1166:AEWVAI%3E2.0.CO;2](https://doi.org/10.1175/1520-0442(2001)014%3C1166:AEWVAI%3E2.0.CO;2), 2001.
- 772 Thorncroft, C. D., Hall, N. M. J., and Kiladis, G. N.: Three-Dimensional Structure and Dynamics of African
773 Easterly Waves. Part III: Genesis, *Journal of the Atmospheric Sciences*, 65, 3596–3607,
774 <https://doi.org/10.1175/2008JAS2575.1>, 2008.
- 775 Tomaziello, A. C. N., Carvalho, L. M. V., and Gandu, A. W.: Intraseasonal variability of the Atlantic Intertropical
776 Convergence Zone during austral summer and winter, *Climate Dynamics*, 47, 1717–1733,
777 <https://doi.org/10.1007/s00382-015-2929-y>, 2016.
- 778 Valcke, S. and Redler, R.: The OASIS Coupler, in: *Earth System Modelling - Volume 3: Coupling Software and*
779 *Strategies*, edited by: Valcke, S., Redler, R., and Budich, R., Springer Berlin Heidelberg, Berlin, Heidelberg, 23–
780 32, https://doi.org/10.1007/978-3-642-23360-9_4, 2012.
- 781 Viltard, A., de Felice, P., and Oubuih, J.: Comparison of the African and the 6–9 day wave-like disturbance patterns
782 over West-Africa and the tropical Atlantic during summer 1985, *Meteorology and Atmospheric Physics*, 62, 91–
783 99, <https://doi.org/10.1007/BF01037482>, 1997.
- 784 Voltaire, A., Exarchou, E., Sanchez-Gomez, E., Demissie, T., Deppenmeier, A.-L., Frauen, C., Goubanova, K.,
785 Hazeleger, W., Keenlyside, N., and Koseki, S.: Role of wind stress in driving SST biases in the Tropical Atlantic,
786 *Climate Dynamics*, 53, 3481–3504, 2019.
- 787 Wade, M., Caniaux, G., and Du Penhoat, Y.: Variability of the mixed layer heat budget in the eastern equatorial
788 Atlantic during 2005–2007 as inferred using Argo floats, *Journal of Geophysical Research: Oceans*, 116, 2011.
- 789 Waliser, D. E. and Graham, N. E.: Convective cloud systems and warm-pool sea surface temperatures: Coupled
790 interactions and self-regulation, *Journal of Geophysical Research: Atmospheres*, 98, 12881–12893,
791 <https://doi.org/https://doi.org/10.1029/93JD00872>, 1993.

- 792 Wallace, J. M., Mitchell, T. P., and Deser, C.: The Influence of Sea-Surface Temperature on Surface Wind in the
793 Eastern Equatorial Pacific: Seasonal and Interannual Variability, *Journal of Climate*, 2, 1492–1499,
794 [https://doi.org/10.1175/1520-0442\(1989\)002%3C1492:TIOSST%3E2.0.CO;2](https://doi.org/10.1175/1520-0442(1989)002%3C1492:TIOSST%3E2.0.CO;2), 1989.
- 795 Wane, D., Lazar, A., Wade, M., and Gaye, A. T.: A Climatological Study of the Mechanisms Controlling the
796 Seasonal Meridional Migration of the Atlantic Warm Pool in an OGCM, *Atmosphere*, 12,
797 <https://doi.org/10.3390/atmos12091224>, 2021.
- 798 Wang, C., Enfield, D. B., Lee, S., and Landsea, C. W.: Influences of the Atlantic Warm Pool on Western
799 Hemisphere Summer Rainfall and Atlantic Hurricanes, *Journal of Climate*, 19, 3011–3028,
800 <https://doi.org/10.1175/JCLI3770.1>, 2006.
- 801 Wang, C., Lee, S.-K., and Enfield, D. B.: Atlantic Warm Pool acting as a link between Atlantic Multidecadal
802 Oscillation and Atlantic tropical cyclone activity, *Geochemistry, Geophysics, Geosystems*, 9,
803 <https://doi.org/https://doi.org/10.1029/2007GC001809>, 2008.
- 804 Webster, P. J., Holland, G. J., Curry, J. A., and Chang, H.-R.: Changes in Tropical Cyclone Number, Duration,
805 and Intensity in a Warming Environment, *Science*, 309, 1844–1846, <https://doi.org/10.1126/science.1116448>,
806 2005.
- 807 Wheeler, M. and Kiladis, G. N.: Convectively Coupled Equatorial Waves: Analysis of Clouds and Temperature
808 in the Wavenumber–Frequency Domain, *Journal of the Atmospheric Sciences*, 56, 374–399,
809 [https://doi.org/10.1175/1520-0469\(1999\)056%3C0374:CCEWAO%3E2.0.CO;2](https://doi.org/10.1175/1520-0469(1999)056%3C0374:CCEWAO%3E2.0.CO;2), 1999.
- 810 Wu, M.-L. C., Reale, O., and Schubert, S. D.: A Characterization of African Easterly Waves on 2.5–6-Day and 6–
811 9-Day Time Scales, *Journal of Climate*, 26, 6750–6774, <https://doi.org/10.1175/JCLI-D-12-00336.1>, 2013.
- 812